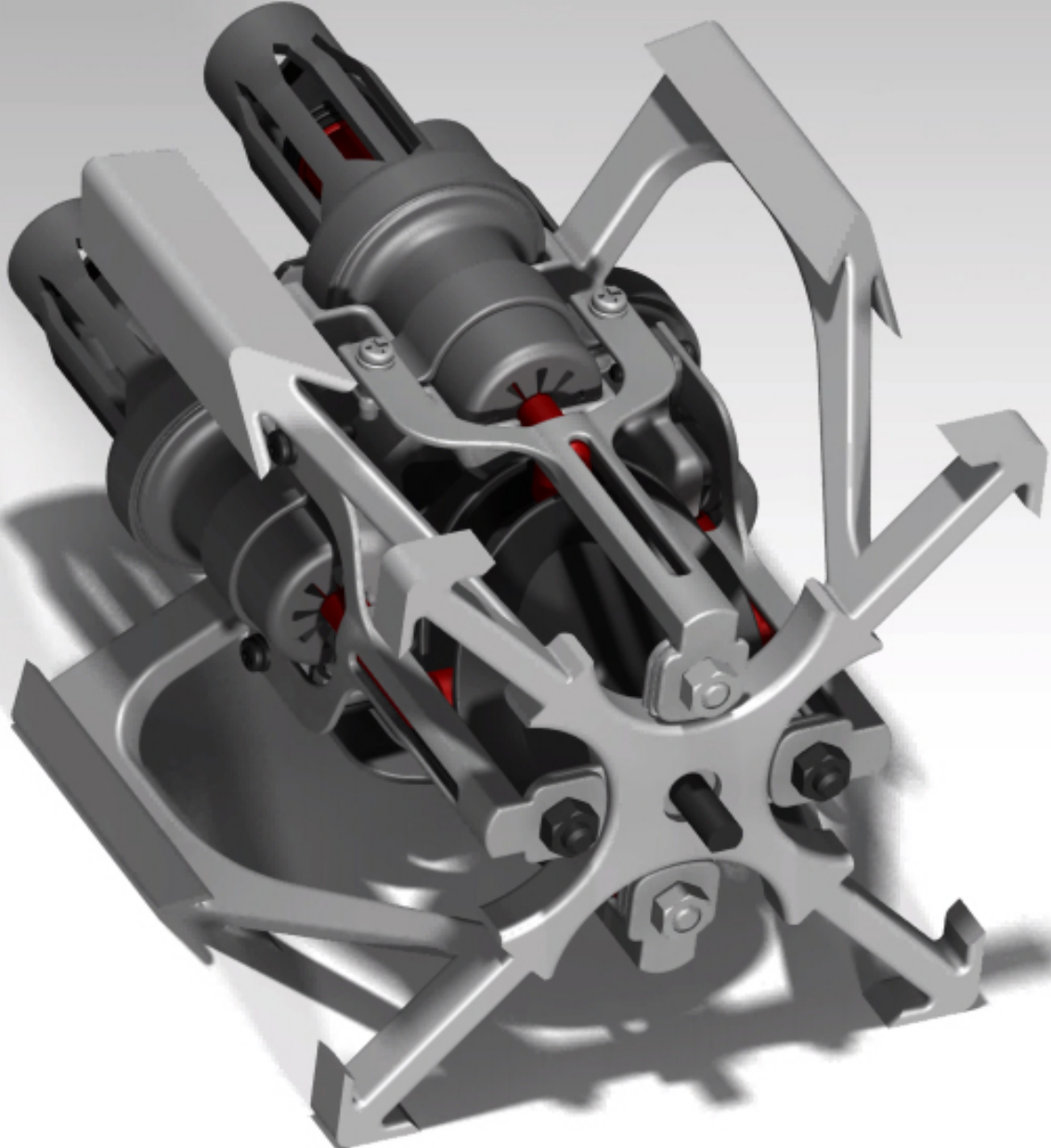


MECH0020 Individual Project

2022/23

Student: SN:	Fadi Zahar 18066190
Project Title:	Novel Hydraulic Actuation System for MRI-Compatible Cardiac Catheterisation Robots: Design and Integration
Supervisor:	Dr. Helge Wurdemann



Declaration

I, Fadi Zahar, confirm that the work presented in this report is my own. Where information has been derived from other sources, I confirm that this has been indicated in the report.

Word Count: 7498 words

Abstract

Cardiovascular diseases, the leading contributor to worldwide mortality, have spurred the adoption of cardiac catheterisation as an effective minimally invasive diagnostic and treatment method. Traditionally, X-ray fluoroscopy is employed to guide these procedures, but it exposes both clinicians and patients to harmful ionising radiations. In recent years, magnetic resonance imaging (MRI) has attracted fast-growing interest as a safer alternative; however, the lack of MRI-compatible actuators hinders robotic interventions under such MRI settings.

This study presents a novel hydraulic actuation system that aims to enable robust robotic teleoperation of MRI-guided catheterisation interventions, thereby eliminating radiation exposure while also improving clinician precision and comfort. The hydraulic motor utilises a four-piston swash plate mechanism within a master-slave configuration and can provide unlimited continuous bidirectional rotation. A combination of 3D printing technologies was used to ensure the production of an entirely MRI-compatible system. Furthermore, fluid dynamics of the hydraulic transmissions were studied to provide design guidelines for the actuation system. To assess the performance of the actuator, positional accuracy and continuous tracking experiments were conducted to evaluate motion replication accuracy. Finally, the motor was integrated into a catheter axial motion unit prototype, and both positional accuracy and continuous tracking were also evaluated for the catheter translation manipulations.

The experimental results demonstrated the successful design of the hydraulic actuator in its applicability for prospective MRI-compatible cardiac catheterisation robots.

Acknowledgements

I would like to extend my sincere appreciation and heartfelt gratitude to my project supervisor and personal tutor, Dr. Helge Wurdemann, for his unwavering support, invaluable guidance, and exceptional patience throughout the entirety of the project. Despite the challenging circumstances caused by the COVID-19 pandemic, Dr. Wurdemann's expertise and supervision have been instrumental in shaping my understanding and achievements. His belief in my work has been a tremendous driving force, motivating me to overcome challenges and consistently strive for excellence.

Lastly, I am forever grateful for the immeasurable support and encouragement provided by my parents, siblings, and family. Their unyielding belief in my abilities and their constant nurturing presence have been a great source of strength and inspiration throughout the completion of this work.

Table of Contents

1. Introduction	13
1.1. Motivation	13
1.1.1. Cardiovascular Diseases and Cardiac Catheterisation Procedures	13
1.1.2. Problems in Existing Catheterisation Procedures	14
1.1.3. MRI's Rise in Popularity and Associated Challenges	15
1.1.4. Statement of Clinical Need	16
1.1.5. MRI Compatibility.....	16
1.2. Aim and Objectives	17
2. Literature Review: Catheterisation Robots, Actuators, and MRI Compatibility.....	18
2.1. Cardiac Catheterisation Robots: State of the Art	18
2.1.1. Conventional Robotic Catheterisation Systems	18
2.1.2. MRI-Compatible Robotic Catheterisation Systems.....	19
2.2. MRI-Compatible Actuation Systems	22
2.2.1. Piezoelectric Actuators.....	22
2.2.2. Pneumatic Actuators	23
2.2.3. Hydraulic Actuators	24
2.3. Summary and Contribution.....	26
3. Design and Integration of a Teleoperated MRI-Compatible Hydraulic Actuation System	28
3.1. Converting Finite Piston Strokes to Unlimited Bi-Directional Rotation.....	28
3.1.1. Fluid Architectures and Preliminary Requirements.....	28
3.1.2. Slave Section: Swash Plate Mechanism.....	29
3.1.3. Kinematics Model.....	32
3.1.4. Master Section: Stepper Motors and Open-Loop Control	33

3.2.	Fluid Dynamics of the Hydraulic Transmission: Governing Equation	35
3.2.1.	Equivalent Transmission Stiffness:.....	37
3.2.2.	System Damping:	37
3.2.3.	Fluid Inertia	37
3.3.	Design Trade-offs and Selection Process.....	38
3.4.	Fabrication and Further Design Considerations.....	39
3.5.	Catheter Axial Motion Unit	40
4.	Experiments, Results, and Discussions.....	42
4.1.	Experimental Setups.....	42
4.1.1.	Hydraulic Motor Rotation Setup.....	42
4.1.2.	Catheter Translation and Cardiac Phantom Assembly.....	43
4.2.	Measuring Performance: Data Collection & Processing.....	45
4.2.1.	Positional Accuracy Experiments.....	45
4.2.2.	Continuous Tracking Experiments.....	46
4.2.3.	Experimental Metrics	48
4.3.	Experiment (A): Hydraulic Motor Rotation: <i>Positional Accuracy</i>	49
4.4.	Experiment (B): Hydraulic Motor Rotation: <i>Continuous Tracking</i>	50
4.5.	Experiments (C): Catheter Translation.....	51
4.5.1.	Experiment (C.1): Axial Motion: <i>Positional Accuracy</i>	51
4.5.2.	Experiment (C.2): Axial Motion: <i>Continuous Tracking</i>	52
4.6.	Discussions.....	53
4.6.1.	Experiments (A)-(B): Hydraulic Motor Rotation	53
4.6.2.	Experiments (C): Catheter Translation	55
5.	Conclusion	57
5.1.	Key Results and Consequences.....	57
5.2.	Limitations and Future Work	57
6.	Bibliography	60
7.	Appendices	70

7.1. Commercially Available Catheterisation Robots	70
--	----

Nomenclature

Abbreviations

CVDs	Cardiovascular Diseases
MI	Minimally Invasive
MRI	Magnetic Resonance Imaging
MR	Magnetic Resonance
FDM	Fused Deposition Modelling
SLA	Stereolithography
EP	Electrophysiology
DNA	Deoxyribonucleic Acid
EM	Electromagnetic
PCI	Percutaneous Coronary Intervention
PVI	Peripheral Vascular Intervention
NVI	Neurovascular Intervention
DOF	Degrees of Freedom
FDA	Food and Drug Administration
RD	Rolling Diaphragm
SNR	Signal-to-Noise Ratio
ROM	Range of Motion
SP	Swash Plate

List of Tables

Table 1: MRI-Compatible Actuation Systems Comparison	27
--	----

List of Figures

Figure 1: A cardiac catheter, represented in light green, is inserted through the patient's groin and guided up to their heart (What Is Cardiac Catheterization, 2022).	13
Figure 2: MRI scanner bore dimensions; adapted from (Salvado et al., 2014).....	16
Figure 3: MRI-compatible catheterisation robot based on ultrasonic motors (Tavallaei et al., 2013).	19
Figure 4: MRI-compatible catheterisation robot based on pneumatic stepper motors (Abdelaziz et al., 2019).	20
Figure 5: MRI-compatible continuous hydraulic motor based on a rotary crankshaft configuration (Dong et al., 2019).	21
Figure 6: Drawing and associated control architecture of a master-slave configuration using hydraulic actuation in an MRI-guided robot-assisted cardiac catheterisation. ...	22
Figure 7: Cylinder pairs balanced and preloaded against one another using rack-and-pinion gearing (top schematic) or timing belts (bottom schematic).	28
Figure 8: Annotated 3D CAD model of the slave section with a close-up on the swash plate at its core (top), along with a real picture of the motor (bottom).	29
Figure 9: CAD models of the slave section (at the top) showing the cross-sections SEC A-A and SEC B-B planes and locations, which are then shown below with proper coordinate axis labelling and numbering of the pistons for reference.....	30
Figure 10: Cross-sections of the motor showing how it replicates the action of the timing belt mechanism, essential to prevent tensile forces on the pistons.	31
Figure 11: 3D CAD model of the swash plate (a) with its geometrical features in both front view (b) and top view (c).	32
Figure 12: Annotated 3D model of both the master and slave sections.	33
Figure 13: Real picture of the master and slave sections along with the open-loop control architecture.	34

Figure 14: Sequence of CCW rotations and associated piston displacements covering a full rotation and assuming the half stroke to be 16mm.....	35
Figure 15: Schematic of a single two-piston fluid line with the associated main dynamics parameters.....	36
Figure 16: Catheter Axial Motion Unit Prototype.....	41
Figure 17: Vertical shot of the disk and the four circular landmarks.....	42
Figure 18: Close-up of the motor and the disk positioned vertically.....	42
Figure 19: Hydraulic motor rotation experiment setup.....	43
Figure 20: Catheter translation experiment setup.....	44
Figure 21: Tracking landmarks for the catheter translation experiment.....	45
Figure 22: Example of positional data retrieval using the 'Ruler' measurement application.....	46
Figure 23: Tracking algorithm flowchart.....	47
Figure 24: Example of boundary box encapsulation for landmark monitoring during manual selection (left; blue box) and monitoring (right; green boxes).....	48
Figure 25: Plot of the mean and SD of the motor's angular position error recorded for different input angles as shown by the disk schematics. An average error of 2.484° was recorded.....	50
Figure 26: Continuous tracking of the motor's angular position through CCW and CW revolutions as shown by the disk schematics. An average error of 1.803° was recorded between input and output.....	51
Figure 27: Plot of the mean and SD of the catheter's absolute axial position error recorded for different axial motion inputs as shown by the artery schematics. An average error of 1.069 mm was recorded.....	52
Figure 28: Continuous tracking of the catheter's axial position through a 100mm insertion and extraction. An average error of 0.784mm was recorded between input and output.....	53
Figure 29: Landmark visibility once entering the phantom artery.....	56

Figure 30: CATIA screenshots showing the initial model (top) vs. the updated model (bottom) where the maximum available half RD/piston stroke was increased from 16mm to 20mm, which consequently extends the length of the motor. 59

Figure 31: Cross-section of the motor with incorporated Rolling Diaphragms..... 59

1. Introduction

1.1. Motivation

1.1.1. Cardiovascular Diseases and Cardiac Catheterisation Procedures

17.9 million people: that is the estimated number of lives claimed by Cardiovascular diseases (CVDs) every year, accounting for nearly one-third of all global deaths (Cardiovascular diseases (CVDs), 2021). These CVDs refer to a group of conditions affecting the heart and blood vessels, including coronary artery disease and arrhythmias, among others (Guttmacher, Collins and Nabel, 2003; Benjamin *et al.*, 2018).

In this regard, cardiac catheterisation has established itself as an effective, minimally invasive procedure to treat and diagnose many of these conditions (Baim, 2007). This endovascular intervention involves the insertion of long flexible instruments, such as catheters and guidewires, into the patient's blood vessel, usually in the groin or arm area, and guiding them to the heart and its vasculature (Figure 1) (Manda and Baradhi, 2023).

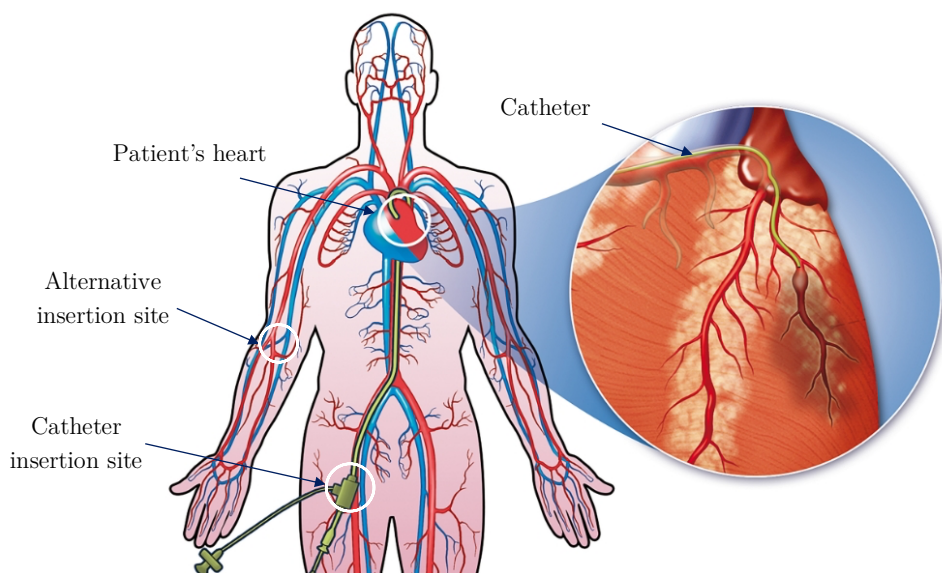


Figure 1: A cardiac catheter, represented in light green, is inserted through the patient's groin and guided up to their heart (What Is Cardiac Catheterization, 2022).

The most common catheterisation procedures include:

- **Coronary Angiography:** A contrast dye is injected through the catheter to detect blockages or narrowing in the coronary arteries using medical imaging technologies. This common procedure helps in diagnosing conditions such as coronary artery disease and determining the need for further interventions like angioplasty or bypass surgery (Baim, 2007; Fihn *et al.*, 2014).
- **Angioplasty and Stenting:** A specialised balloon catheter is used to open blocked arteries by inflating a balloon at its tip when reaching the blockage location. Stents, which are small mesh tubes, are often placed at the site to maintain the artery's openness and improve blood flow (Moses *et al.*, 2003).
- **Electrophysiology (EP) Study and Ablation:** During an EP study, catheters with electrodes are positioned within the heart to assess electrical activity and locate the source of abnormal heart rhythms. Once identified, catheter ablation can be performed to eliminate the abnormal tissue causing the arrhythmia (Calkins *et al.*, 2012).
- **Valvuloplasty and Valve Replacement:** Valve-related conditions are treated by dilating narrowed heart valves (valvuloplasty) using a balloon catheter or replacing damaged valves (Holmes *et al.*, 2012).

1.1.2. Problems in Existing Catheterisation Procedures

During cardiac catheterisation procedures, immediate visual feedback is essential for interventionalists to accurately navigate and manipulate the instruments within the patient's heart and blood vessels. Traditionally, X-ray fluoroscopy has been the primary imaging modality for these procedures. However, this technique exposes both patients and clinicians to ionising radiation (Lange and Von Boetticher, 2006), which can damage DNA and pose a risk for cancer development (Goldman, 1982; Modan *et al.*, 2000; Prasad, Cole and Hasse, 2004; Chambers *et al.*, 2011). This exposure is particularly

concerning for clinicians who, throughout their careers, perform hundreds of such procedures.

To mitigate radiation exposure, clinicians employ shields and wear cumbersome equipment, including lead aprons, while also minimising the time and frequency of exposures (Kim and Miller, 2009; Badawy *et al.*, 2016). Despite these precautions, clinicians still face elevated cancer risks (Venneri *et al.*, 2009). Moreover, the heavy protective gear can lead to physical strain and a higher likelihood of developing orthopaedic-related issues (Ross *et al.*, 1997; Orme *et al.*, 2015).

1.1.3. MRI's Rise in Popularity and Associated Challenges

The rising number of cardiac catheterisations, with over a million interventions performed each year in the United States alone (Slicker *et al.*, 2016), highlights the need to explore alternative imaging techniques to minimise radiation hazards. Magnetic Resonance Imaging (MRI) has emerged as an increasingly popular alternative to X-ray fluoroscopy, primarily due to its ability to eliminate ionising radiation exposure (Muthurangu and Razavi, 2005). Furthermore, MRI offers a more versatile multiparameter imaging modality, creating high-contrast 3D visualisations of soft tissue which is not possible with the 2D projections provided by X-ray fluoroscopy (Krieger *et al.*, 2012). This advantage is especially important for ablation procedures (Green *et al.*, 2005; Shokrollahi *et al.*, 2011; Muller *et al.*, 2012).

Despite its benefits, MRI scanners are imposing tubular machines (Figure 2) making it difficult for clinicians to access catheter manipulation sites as they need to reach into the bore of the scanner to treat the patient (Fernández-Gutiérrez *et al.*, 2015).

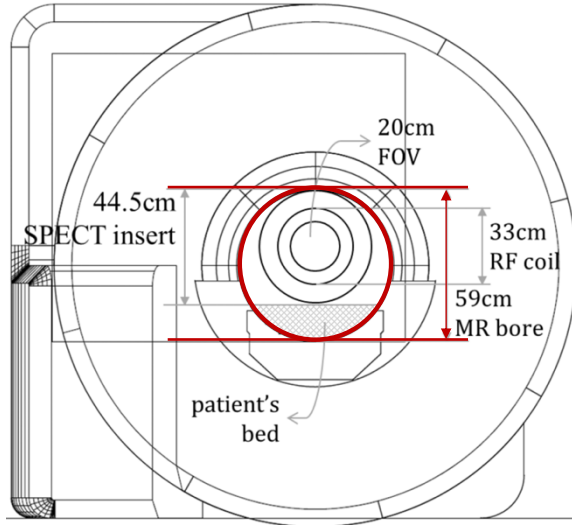


Figure 2: MRI scanner bore dimensions; adapted from (Salvado et al., 2014).

These challenging ergonomics have been directly linked to the discomfort experienced by clinicians, becoming even more problematic when operating on small children (Krueger *et al.*, 2006).

1.1.4. Statement of Clinical Need

Given the concerns highlighted, there has been an increasing interest in teleoperated robotic platforms to perform MRI-guided catheterisation procedures (Abdelaziz *et al.*, 2019), as they eliminate radiation exposure for everyone involved while enhancing procedural comfort, and reproducibility.

1.1.5. MRI Compatibility

The primary obstacle to transitioning to MRI-guided interventions lies in the scarcity of MRI-compatible actuators in a world dominated by electric motors. Here, ‘MRI-compatibility’ is defined as the characteristic of a device that enables its safe use within an MRI environment, without its operation being negatively impacted by the MRI

system while maintaining the imaging quality (Fischer *et al.*, 2008a; Su *et al.*, 2022). This entails constructing the device using non-magnetic materials to prevent interference with MRI scans' magnetic field of 0.5 to 1.5 Tesla (Berger, 2002). Failure to do so could lead to image artefacts, field distortion, or compromise the safety of the patient and medical staff (De Wilde *et al.*, 2007; Monfaredi, Cleary and Sharma, 2018; Panych and Madore, 2018).

However, conventional “off-the-shelf” motors and robotic components, are not MRI-compatible due to ferromagnetic materials and the electromagnetic (EM) interference they generate which constitutes the primary challenge to overcome.

1.2. Aim and Objectives

This study aims to design, build, and test an MRI-compatible actuation system that can be integrated into a catheterisation robot, enabling robust teleoperation.

The objectives of the study are summarised as follows:

- 1) Develop a robust actuation system that allows for teleoperated, continuous, unlimited, bidirectional rotation.
- 2) Construct the actuation system entirely using MRI-compatible materials.
- 3) Test the actuator's performance through a series of positional accuracy and continuous tracking experiments.
- 4) Design a catheter axial motion unit prototype that can accommodate typical cardiac catheter sizes and integrate the actuator into it.
- 5) Assess the actuator's performance in terms of catheter translation manipulations after its integration into the catheter axial motion unit prototype.
- 6) Compare the results from 5) with conventional remote catheter navigation performance.

2. Literature Review: Catheterisation Robots, Actuators, and MRI Compatibility

2.1. Cardiac Catheterisation Robots: State of the Art

In recent years, there has been a surge of interest in robotic catheterisation, driven by the enhanced safety, precision, and accuracy they offer. This has sparked the development of a wide variety of both research prototypes and commercially available systems (Maor *et al.*, 2017; Zhao *et al.*, 2022).

2.1.1. Conventional Robotic Catheterisation Systems

To date, all commercially available catheterisation robotic systems have been designed to work under X-ray fluoroscopy guidance. Among these systems are the *CorPath® GRX* platform (Corindus, Inc.) as well as the *Sensei®* and *Magellan* platforms (Hansen Medical, Inc). Additional systems include the *Amigo™ RCS* (Catheter Precision, Inc.), the *Robocath R-One™* (Robocath), and the *Niobe® ES Magnetic Navigation System* (Stereotaxis, Inc.). Only a summary in terms of their relevance for this study is provided below; however, if the reader is interested in a comprehensive overview of each system, Appendix 7.1. provides further information.

When it comes to MRI-guided procedures, all of these commercial platforms are not MRI-compatible due to their use of electric servo motors or, in the case of the *Niobe® ES*, a magnetic actuation system that provides steering torques directly at the custom-made catheter's tip.

As for the instrument handling mechanisms, the roller-based design, as seen in the *CorPath® GRX* or *R-One™*, is considered the most effective. This mechanism, used to

concentrically clamp catheters/guidewires, offers precision control over an unlimited range, making it particularly convenient (Najafi et al., 2023).

2.1.2. MRI-Compatible Robotic Catheterisation Systems

While these systems remove clinicians from ionising radiation exposure, the patient remains unprotected from the X-rays. This presents a direct limitation for paediatric catheterisation procedures, where such exposure is not recommended or even possible (Thukral, 2015). Several research groups have therefore focused their attention on developing MRI-compatible robotic catheterisation systems:

Tavallaei et al. (2013) introduced a magnetic-resonance-compatible remote catheter navigation system (MR-RCNS) based on **ultrasonic motors**—a type of **piezoelectric actuator**—made of non-ferromagnetic materials (Figure 3). The catheter is translated using a set of motor-driven rollers incorporated in a rotating setup. The experiments demonstrated a maximum time delay of $41 \pm 21\text{ms}$ in replicating motion, with absolute errors of $2 \pm 2^\circ$ (peaking at 6°) for catheter radial motion over 360° and $1.0 \pm 0.8\text{mm}$ (peaking at 2.8 mm) for catheter axial motion over 100 mm.

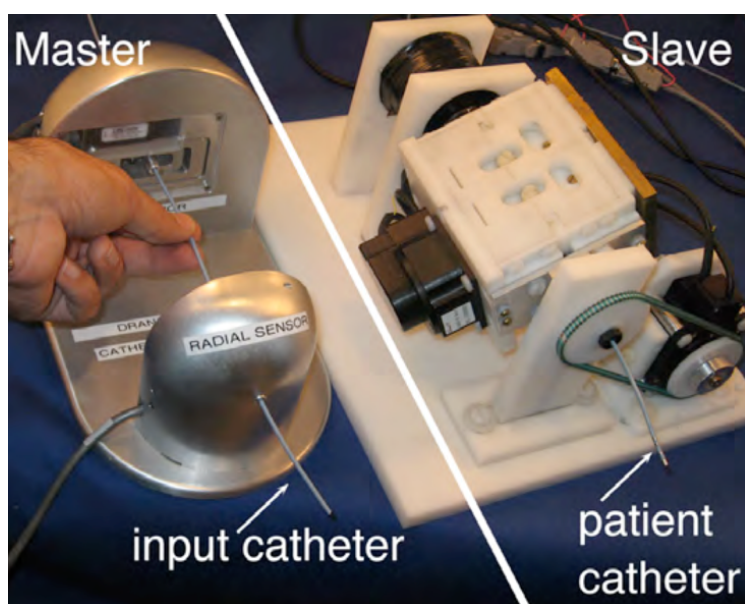


Figure 3: MRI-compatible catheterisation robot based on ultrasonic motors (Tavallaei et al., 2013).

More recently, Abdelaziz et al. (2019), developed a novel teleoperated robotic platform for catheterisation procedures, which employs **pneumatic stepper motors** and integrates a user-friendly interface with haptic feedback (Figure 4). The robot is capable of carrying out translational and rotational movements of standard catheters/guidewires. The mechanism involves repeated cycles of clamping and translating and uses both linear and rotational pneumatic stepper motors. The former has a positional accuracy of 0.1mm, and the latter a positional accuracy of 1° (Groenhuis and Stramigioli, 2018; Groenhuis, Siepel and Stramigioli, 2018). A study involving clinical experts demonstrated success rates of 90%-100% and supported the robot's dexterity in using pneumatic actuation (Kundrat et al., 2021).

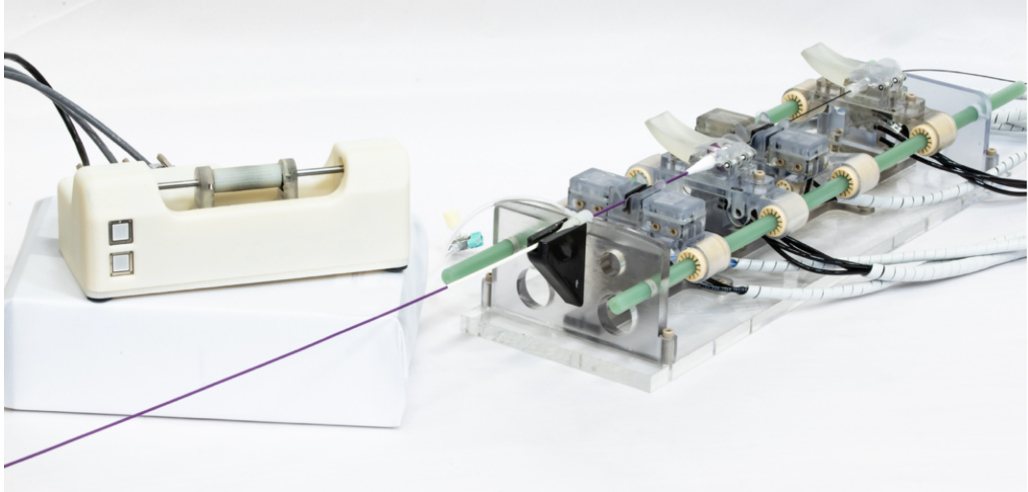


Figure 4: MRI-compatible catheterisation robot based on pneumatic stepper motors (Abdelaziz et al., 2019).

Lastly, Lee et al. (2018) engineered an MRI-compatible catheter tele-manipulator powered by **hydraulic actuation**, a first of its kind. The system uses rolling diaphragms (RDs)—flexible, hat-shaped, elastomeric membranes—as a replacement for the conventional high-friction O-ring seals. Each actuation unit consists of two RD-sealed cylinders whose threaded pistons are linked in rack-gear antagonist configurations, enabling rotation over a limited range. Experimental evaluations demonstrated successful results with motion replication under 70ms at 15Hz, a peak output torque of

1.47Nm, low hysteresis of 1.29mm at 0.1Hz, and small mechanical backlash of 0.88mm, among others.

In an effort to improve the system's performance and its limited range, a continuous hydraulic motor based on adapted RD-sealed cylinders was also developed and integrated (Dong *et al.*, 2019). The design incorporates three RD-sealed cylinders arranged in a rotary crankshaft configuration and placed radially at 120° intervals (Figure 5). Moreover, novel control methods based on kinematics models and more advanced techniques were also introduced (Wang *et al.*, 2018; Dong *et al.*, 2022).

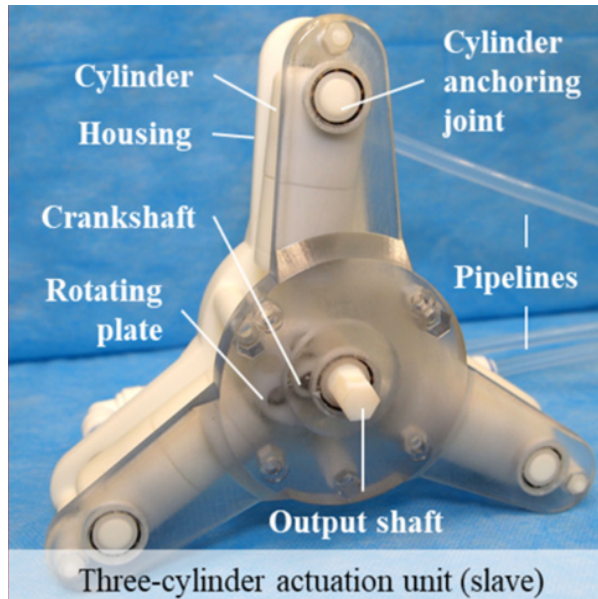


Figure 5: MRI-compatible continuous hydraulic motor based on a rotary crankshaft configuration (Dong et al., 2019).

All the above-mentioned teleoperated MRI-compatible systems are based on an effective master-slave configuration. The latter refers to a type of teleoperation system in which a device (the master) takes inputs from an operator to control another device (the slave) (Aliaga, Rubio and Sánchez, 2004). In the context of robotic catheterisation, the master is usually the control unit manipulated by the clinician, often located far from the operating room, while the slave is the robotic system situated next to the patient, directly controlling the catheter (Figure 6).

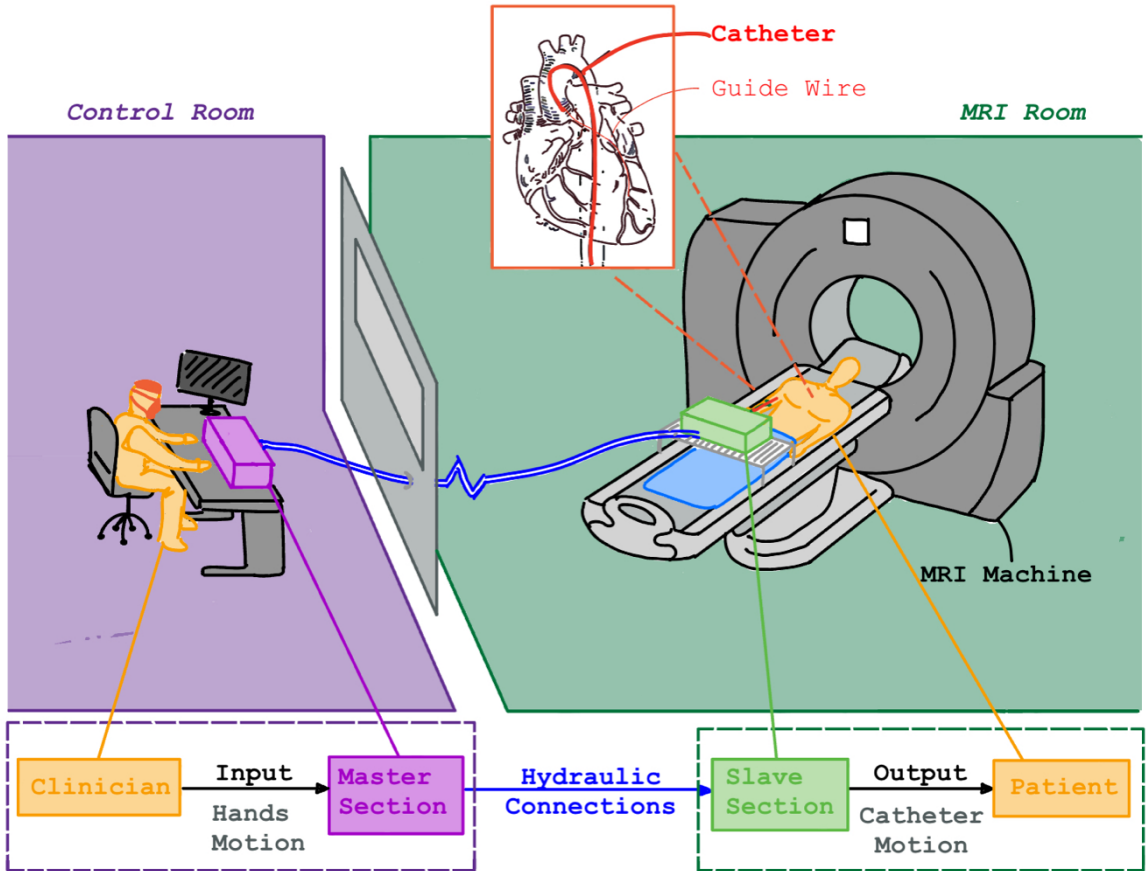


Figure 6: Drawing and associated control architecture of a master-slave configuration using hydraulic actuation in an MRI-guided robot-assisted cardiac catheterisation.

2.2. MRI-Compatible Actuation Systems

Following section 2.1.2., three main types of MRI-compatible actuators can be distinguished: **piezoelectric**, **pneumatic**, and **hydraulic**. These are discussed in the sections below.

2.2.1. Piezoelectric Actuators

The first MRI-guided robotic system is credited to Masamune et al. (1995) who used piezoelectric ultrasonic motors to operate stereotactic neurosurgery. Piezoelectric actuators are sophisticated devices that convert electrical energy to mechanical energy

in the form of controlled mechanical displacements based on the inverse piezoelectric effect (Adriaens, De Koning and Banning, 2000).

Known for their high precision, accuracy, speed, and compactness, these actuators are attractive options for catheterisation procedures. Moreover, unlike conventional EM motors, they produce no magnetic field (Spanner and Koc, 2016). However, without appropriate shielding equipment, commercially available piezoelectric motors and their drivers do cause EM interference, and have to be placed at a distance from the MRI scanner (Fischer *et al.*, 2008b; Krieger *et al.*, 2013). These actuators and drivers can lead to a significant reduction in the Signal-to-Noise Ratio (SNR) of MRI images, often ranging between 40%-80% as demonstrated in an MRI-compatibility study involving ultrasonic motors (Fischer *et al.*, 2008b).

Several studies investigated custom-made components and EM-shields to minimise EM interference (Carvalho *et al.*, 2020). Another focus has been on customising the motor driver to mitigate noise and related signal loss under imaging, with Su *et al.* (2012) having achieved a low SNR loss of 2%.

These investigations highlight several measures to substantially reduce electrical noise, thereby providing MRI compatibility (Fischer, Cole and Su, 2011; Su *et al.*, 2016; Patel *et al.*, 2019, 2020; Carvalho *et al.*, 2020; Li *et al.*, 2021).

2.2.2. Pneumatic Actuators

Fluid-driven motors such as pneumatic and hydraulic actuators which use pressurised air and incompressible liquid respectively, prevent the introduction of electrical noise, making them inherently MRI-compatible. Furthermore, pneumatic systems have been considered especially attractive for being inherently safe as any leak is just harmless air which can be easily refilled with medical-grade compressed air.

Pneumatic stepper motors offer precise motion control without relying on closed-loop feedback mechanisms, making them a reliable solution in MRI-guided procedures. Stoianovici et al. (2007) were the first to create a *pneumatic stepper motor* (PneuStep) based on a “hoop gear” driven through the pressurisation of three integrated ports. It is entirely made of a combination of plastics, ceramics, and elastomers, ensuring its suitability for MRI-guided interventions (Stoianovici, Song, *et al.*, 2007). The novel actuator achieved easy-to-control positioning repeatability of $0.076 \pm 0.035\text{mm}$ and operates through 7-metre-long hoses. However, PneuStep is limited by its discrete positioning, having a 3.33° step angle, which is almost twice the 1.8° step angle of a normal electric stepper motor such as the NEMA17.

However, the application of pneumatic stepper motors in more dynamic procedures such as EP catheterisation, which demands responsive instrument manipulation, is more challenging. This is primarily due to the high compressibility of pneumatics which leads to low-stiffness transmissions and limited force/torque outputs, making it difficult to maintain minimal time delays. Additionally, the operation of these systems can introduce non-negligible noise and vibrations, especially if not properly managed in terms of air dissipation and valve-activated pressure/flow regulations. This issue, compounded by the inherent acoustic noise of 82-120 decibels (Price *et al.*, 2001) produced by the MRI scanner, may contribute to discomfort and anxiety (Quirk *et al.*, 1989), especially for paediatric patients (Budinger and Bird, 2018).

2.2.3. Hydraulic Actuators

Hydraulic actuation, which uses an incompressible liquid such as water or oil, offers distinct advantages over pneumatic counterparts. Due to the incompressibility of the liquid, hydraulic systems provide significantly faster, more precise, and more responsive motion control. Moreover, their high power density means that they can be made smaller

than pneumatics motors while achieving the same power output (Ganesh *et al.*, 2004; Lindenroth *et al.*, 2016).

However, hydraulic actuation can be prone to leaks which might seriously hinder its operation. Risks of seal degradation and fluid contamination are also a concern but can be prevented through regular maintenance. From a performance perspective, the typical rubber O-ring seals may introduce large Coulomb friction which results in nonlinearities and mechanical losses. However, new sealing methods such as moulded fabric-reinforced elastomeric Rolling Diaphragms (RD) claim to provide leak-proof sealing and considerably reduce the friction of the system.

Whitney *et al.* (2016) used pairs of RD-sealed metallic cylinders to engineer high-stiffness pressurised fluid transmissions and form efficient rotary hydraulic actuators with a 135° range of motion (ROM). This system, adapted from their previous work (Whitney *et al.*, 2014), employs cylinder pairs balanced against one another using timing belts. The RDs greatly reduced friction and enhanced mechanical performance.

Guo *et al.* (2018) also developed a compact robot for MRI-guided bilateral stereotactic neurosurgery which is powered by hydraulic actuators with a 201.2° ROM. The latter uses RD-sealed cylinders in similar rack-gear antagonist arrangements as previously seen in (Lee *et al.*, 2018). The robot achieved satisfactory needle insertion targeting accuracy with an average of under 1.73mm.

Finally, the actuators above-mentioned are bound to restricted ROMs due to the nature of the rack-gear and timing belt configurations, combined with the limited RD strokes. Although increased motion ranges can be made possible by gearing down the actuator, this unavoidably compromises both the torque output as well as the durability of the components, especially when made with non-metallic MRI-compatible materials. This led Dong *et al.* (2019) to create the continuous, unlimited, bidirectional hydraulic

motor mentioned in section 2.1.2. earlier. The motor respectively achieved fast step responses under 40ms, small time delays of 60ms at 1Hz, and an input-output error of 0.64° in average (peaking at 1.5°) under sinusoidal positional tracking at 0.05Hz.

2.3. Summary and Contribution

As highlighted in section 1.1.5., the most significant challenge in developing and deploying robots for MRI-guided interventions lies in the design of compatible actuation systems. For their high dynamic performance, inherent MRI-compatibility, and simplicity, hydraulics was chosen as the preferred actuation method. This decision was made after comparing them to piezoelectric motors, which require extensive precautions to achieve MRI compatibility, and pneumatic motors, which lag in terms of dynamic performance (Table 1).

The rest of this study will therefore explore the design and fabrication of a hydraulic motor in a master-slave configuration, with the ultimate aim to accelerate the transition to MRI-guided interventions.

Table 1: MRI-Compatible Actuation Systems Comparison

	<i>Piezoelectric Actuators</i>	<i>Pneumatic Actuators</i>	<i>Hydraulic Actuators</i>
Pros	<ul style="list-style-type: none"> • High precision, accuracy, speed, and compactness. 	<ul style="list-style-type: none"> • Inherently MRI-compatible. • No electrical noise interference. • Harmless air leaks, easily refilled in hospitals. • Easy maintenance 	<ul style="list-style-type: none"> • Inherently MRI-compatible. • No electrical noise interference. • High power density • Accurate, fast, and responsive
Cons	<ul style="list-style-type: none"> • EM interference due to typical high metal content. • Source of significant noise affecting imaging quality. • Requires extensive measures to ensure MRI compatibility. 	<ul style="list-style-type: none"> • Major dynamics challenges due to air's compressibility, affecting position control and speed with low positional accuracy and considerable time delays. • Low power density • Acoustic noise and vibrations introduced, causing patient discomfort and anxiety. 	<ul style="list-style-type: none"> • Potential fluid leaks cause serious risks: can damage surrounding equipment and considerably affect performance. • High maintenance • High friction related to conventional O-ring seals.

3. Design and Integration of a Teleoperated MRI-Compatible Hydraulic Actuation System

The details of the hydraulic motor design and its integration for catheter translation will be explored in the subsequent sections.

3.1. Converting Finite Piston Strokes to Unlimited Bi-Directional Rotation

3.1.1. Fluid Architectures and Preliminary Requirements

Hydraulic transmissions fundamentally *cannot* support tensile forces. In a two-piston setup, tension on one piston reduces fluid pressure, thus requiring a counter force on the other piston. Without it, air might enter through leaks, making the fluid compressible and possibly causing cavitation, or vapor bubble formation (Buerger, 2005). To mitigate this, one effective approach is to preload pairs of antagonistic cylinders against each other using a timing belt or rack-and-pinion gear setup as seen in (Whitney *et al.*, 2014, 2016; Lee *et al.*, 2018) and depicted in Figure 7. With this configuration, actuating one piston initiates movement in the other three, enabling bidirectional action of all pistons.

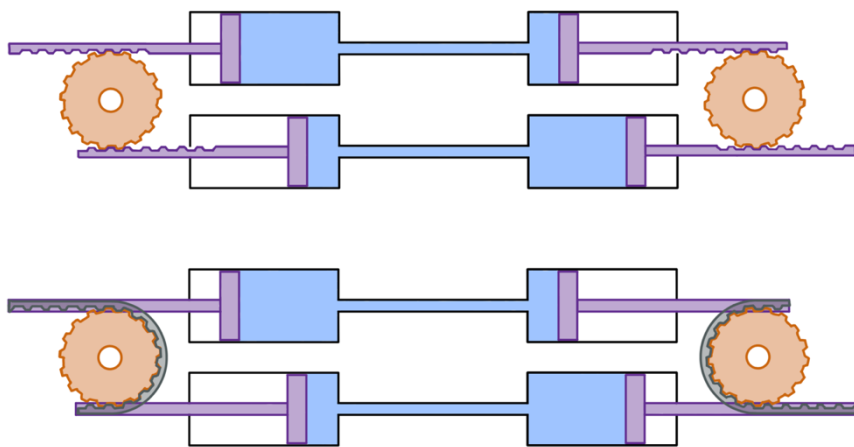


Figure 7: Cylinder pairs balanced and preloaded against one another using rack-and-pinion gearing (top schematic) or timing belts (bottom schematic).

Such ‘mechanical loop’ always ensures the exertion of compressive (push) forces against the pistons and prevents tensile (pull) forces to be introduced.

3.1.2. Slave Section: Swash Plate Mechanism

This study's crux and novelty lie in the design of the slave section, which must mimic a motor's function by enabling continuous, unlimited bidirectional rotation. Drawing inspiration from swash plate piston pumps, a novel swash plate (SP) mechanism is introduced (Figure 8). This mechanism transforms the uniaxial strokes of four pistons (in red) into the rotation of a shaft, specifically, the swash plate's D-shaped end.

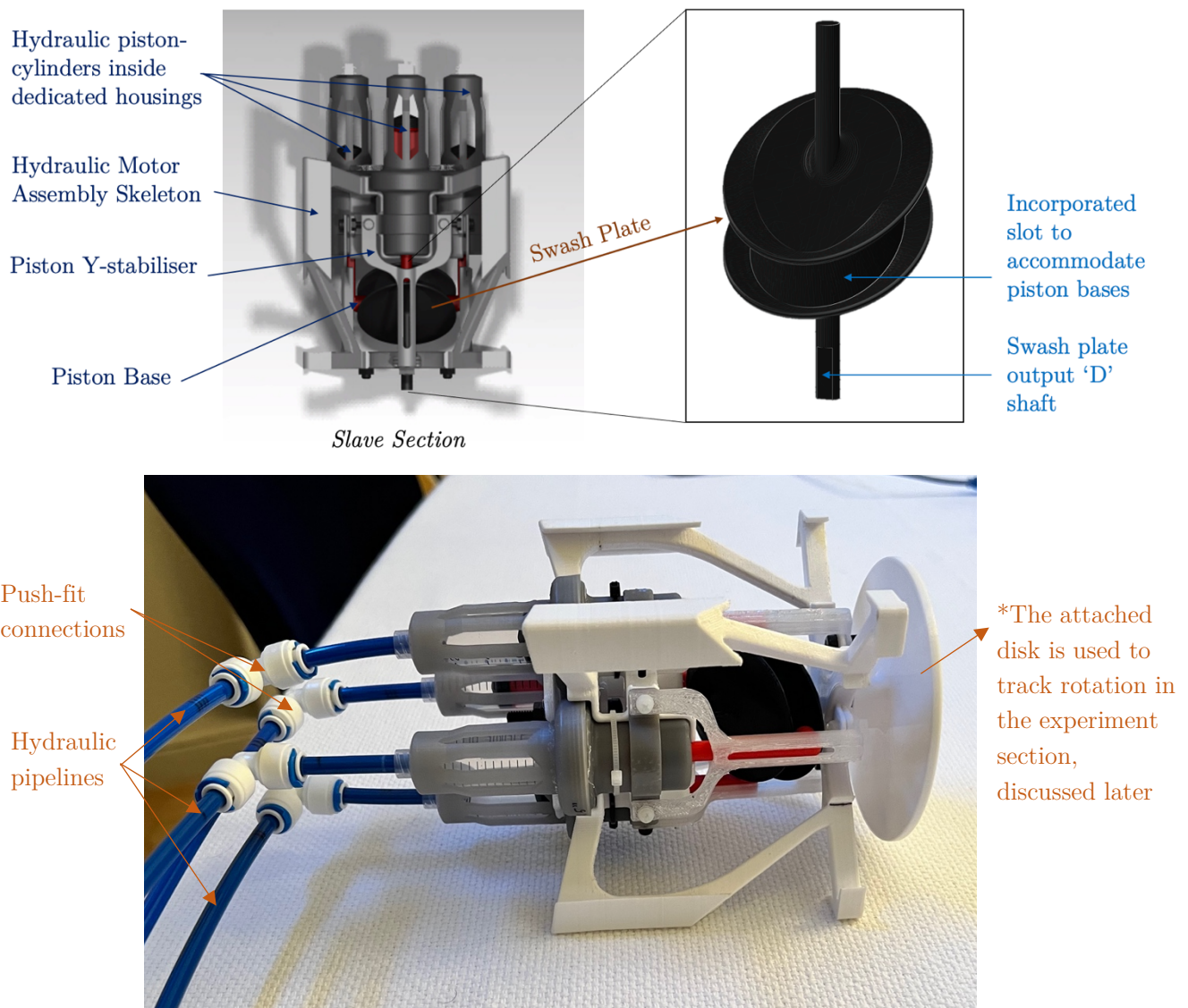


Figure 8: Annotated 3D CAD model of the slave section with a close-up on the swash plate at its core (top), along with a real picture of the motor (bottom).

Figure 9 shows two perpendicular cross-sections of the motor at a specific configuration and captures the positions of the four pistons. These latter are grouped in antagonistic pairs of pistons p1-p3 and pistons p2-p4, respectively balancing against one another, all within an interconnected configuration. In this figure, piston p1 is positioned at the down-stroke position, which inherently places piston p3 at the up-stroke position. Similarly, pistons p2 and p4 are both positioned at the neutral plane position.

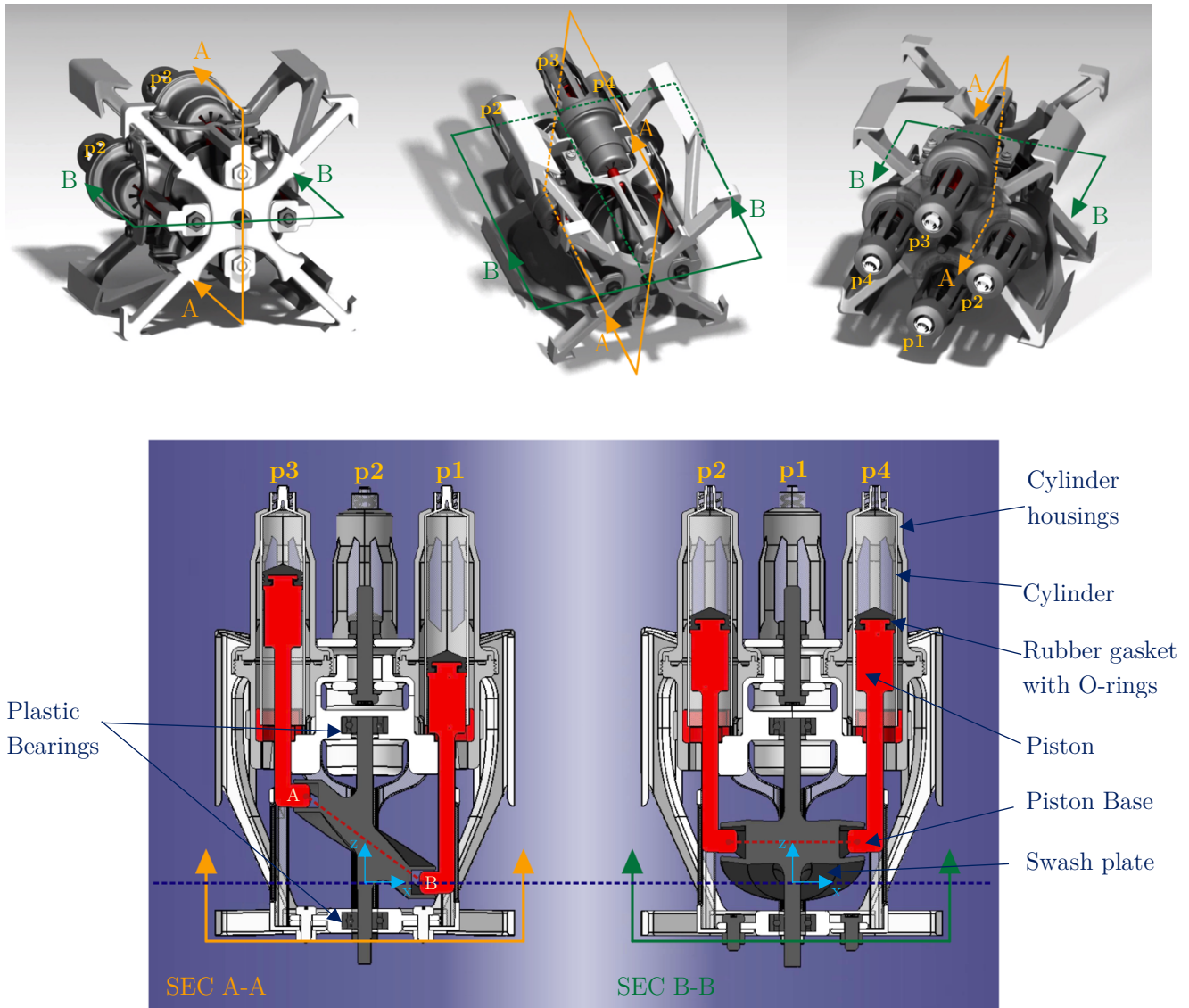


Figure 9: CAD models of the slave section (at the top) showing the cross-sections SEC A-A and SEC B-B planes and locations, which are then shown below with proper coordinate axis labelling and numbering of the pistons for reference.

Indeed, leveraging its unique design, the SP mechanism amplifies the advantages described for the timing belt or rack-and-pinion gear arrangements (Figure 10),

extending them in 3D. The SP allows for the integration of double the number of pistons: two pairs, each made out of diametrically opposed antagonist pistons, with all cylinders situated around the swash plates at 90° intervals. Importantly, this mechanism integrates these pistons to enable unlimited, bidirectional rotation through meticulously synchronised movements of these pistons, the details of which will be addressed in the subsequent sections.

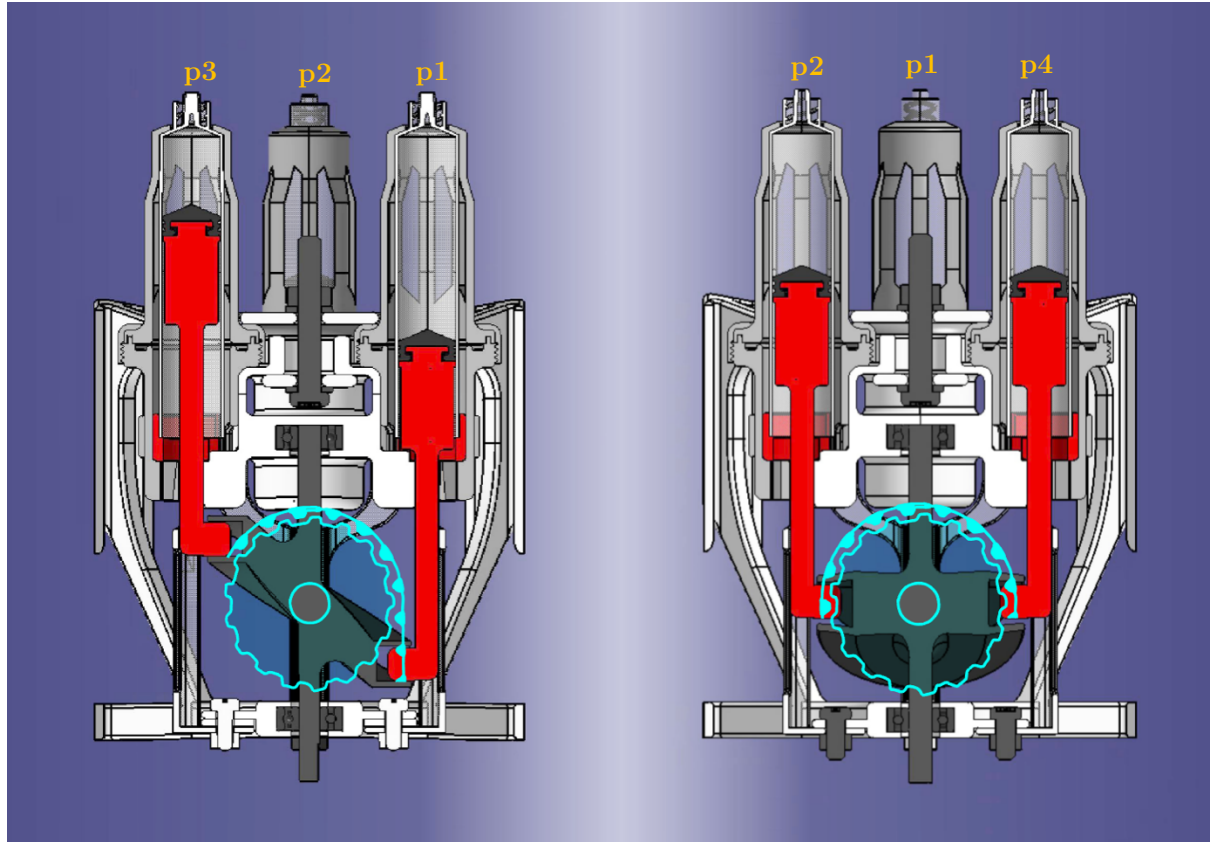


Figure 10: Cross-sections of the motor showing how it replicates the action of the timing belt mechanism, essential to prevent tensile forces on the pistons.

On the other hand, contrasting with the hydraulic motor developed by Dong et al. (2019) which employs a rotary crankshaft configuration where cylinders are arranged radially (Figure 5), the swash plate mechanism offers higher compactness by grouping the cylinders together with their axes parallel to one another and to the motor shaft. Such compactness is particularly important given the spatial limitations inherent to MRI scanners. Moreover, in this design, the cylinders remain stationary, with only the pistons and swash plate in motion during operation. This feature minimises equipment wear

and, in case RDs are incorporated, ensures sufficient clearance between the cylinder and the piston to prevent convolution-related tearing. This contrasts with the above-mentioned motor where the cylinders, pivoted on a ceramic bearing at one end, swing during crankshaft rotation.

3.1.3. Kinematics Model

The kinematics of the slave mechanism are deduced from the swash plate geometry, which resembles an ellipse tilted along its minor axis, and appearing as a circle when viewed from the top. This is depicted in Figure 11, where α represents the major axis of

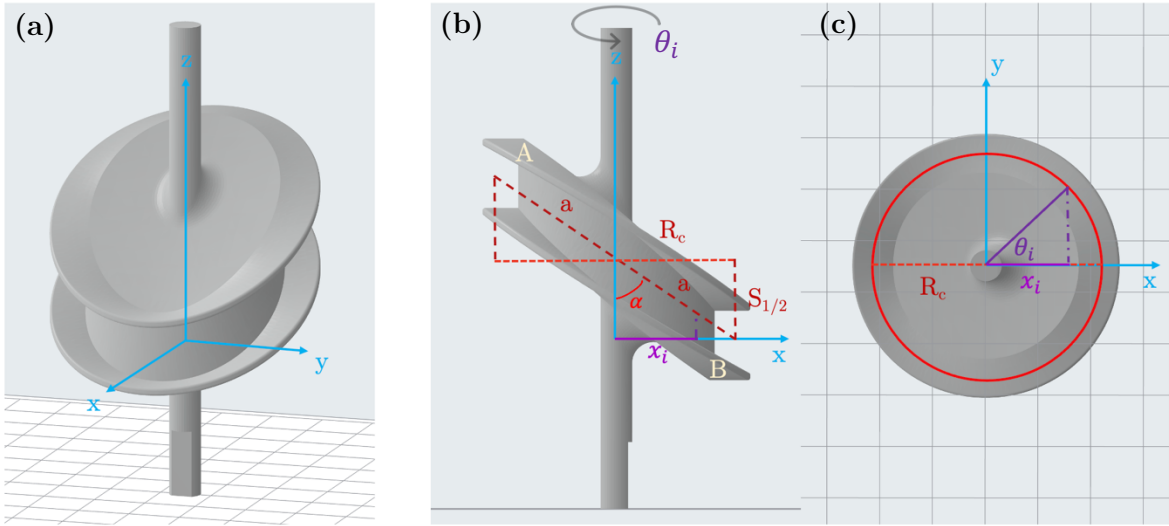


Figure 11: 3D CAD model of the swash plate (a) with its geometrical features in both front view (b) and top view (c).

the ellipse, α the tilt angle, $R_c = \alpha \cdot \cos(\alpha)$ the top-view ‘circle’ radius, and $S_{1/2} = \alpha \cdot \sin(\alpha)$ half the available piston stroke. Points A and B symbolise the centroids of the base of two diametrically opposed pistons p3-p1 attached to the SP, also shown in Figure 9. By combining both geometries from views (b) and (c)—through the x-coordinate—to evaluate the effect of SP rotations θ_i (relative to the z-axis) on the height z describing the displacement of piston p1, it can be shown that:

$$z_1(\theta) = S_{1/2} \cdot (1 - \cos\theta) \quad \text{Eq. (1)}$$

This equation relates the displacement z_1 of p1 to the angular position θ of the SP defined as zero at this ‘base’ configuration and positive counter-clockwise (CCW). As the pistons are evenly placed around the SP, the displacement of the other three pistons p2-p3-p4 can be derived from Eq. (1) by adding associated phase differences. The equation for the i^{th} cylinder becomes:

$$z_i(\theta) = S_{1/2} \cdot (1 - \cos(\theta + \varphi_i)) \quad \text{Eq. (2)}$$

Where $\varphi_i = \frac{2\pi}{n} \cdot (i - 1) = \frac{\pi}{2}(i - 1) \text{ rad}$ is the phase with n equal to the total number of cylinders which is 4 in our case.

3.1.4. Master Section: Stepper Motors and Open-Loop Control

The master-slave configuration, as depicted in Figure 12, consists of four closed fluid lines formed by pistons p1-p1', p2-p2', p3-p3', and p4-p4'. The ‘master’ pistons p1'-p2'-p3'-p4' are actuated by two off-the-shelf leadscrew NEMA17 stepper motors (Sainsmart

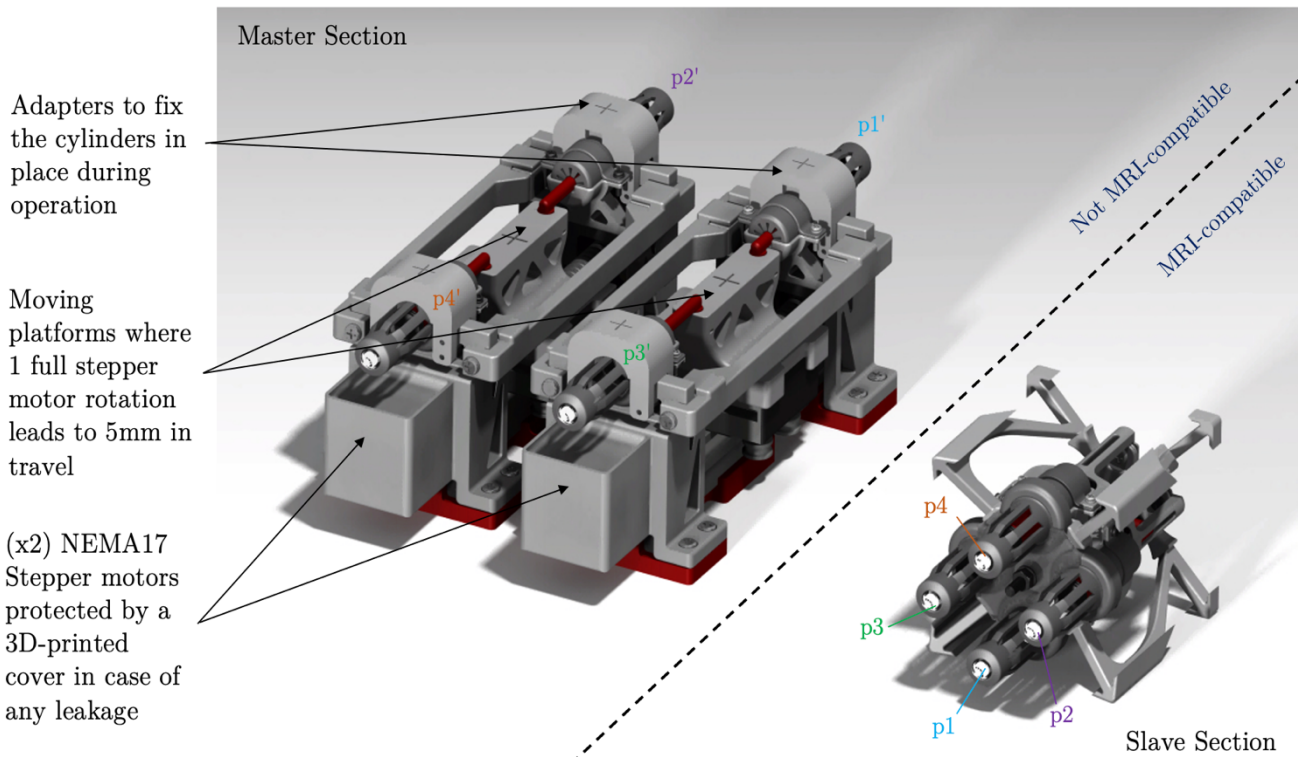
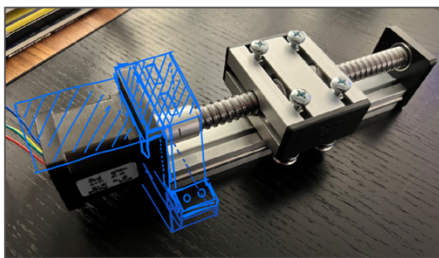


Figure 12: Annotated 3D model of both the master and slave sections.

Ltd.). Pistons p_{1'}-p_{3'} and p_{2'}-p_{4'} are grouped together, taking advantage of the system's antagonistic nature where the displacements z_i and z_{i+2} ($i = 1, 2$) are 180° out of phase. The stepper motors, powered by a 24V power supply, are open-loop controlled using two Microstep stepper motor drivers with a resolution of 3200 microsteps/revolution, both connected to an Arduino Mega 2560 (Figure 13). Using Eq. (2), the motors control the strokes of the pistons based on the desired angular position, θ , to be reached by the motor's shaft. It is worth noting that θ can describe any function that varies over time.

(x2) leadscrew stepper motors (see picture below before integration)—programmed to follow precise sinusoidal motions leading to the rotation of the Swash Plate



(x2) Microstep stepper motor drivers (accepting 9~42VDC) with a 16-microstep resolution, equivalent to 3200 microsteps for 1 motor revolution

24V output power supply

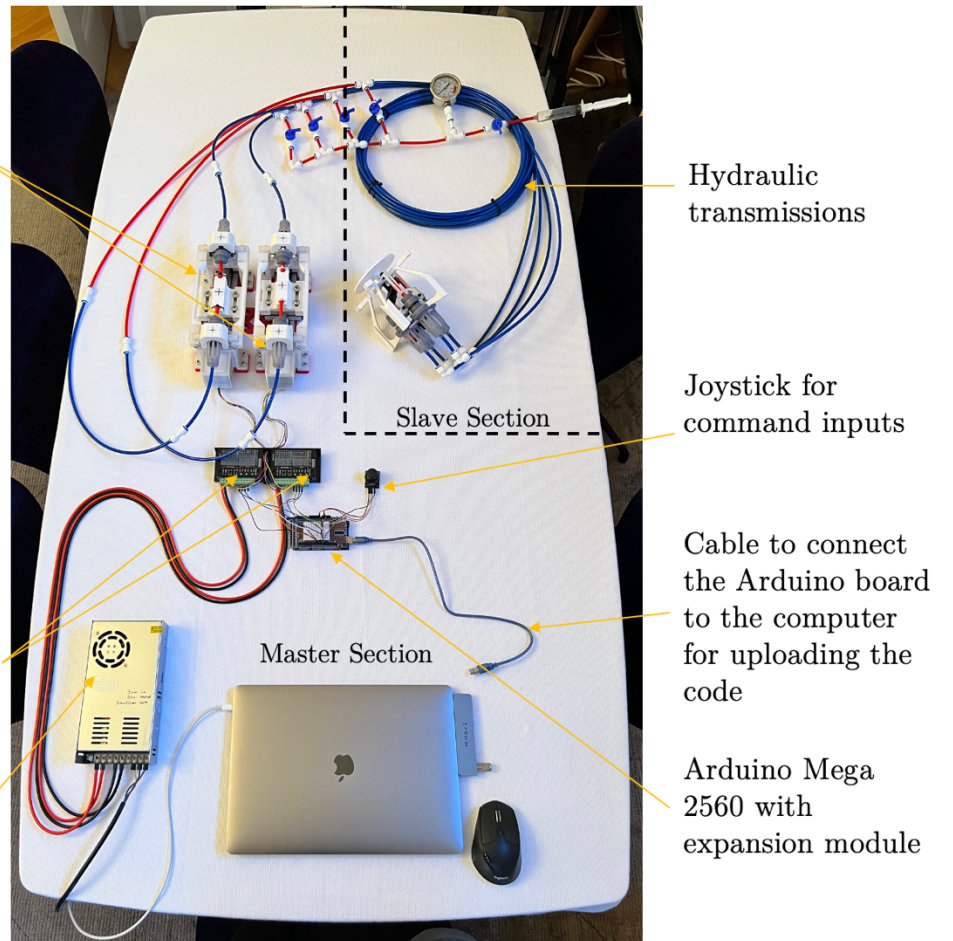


Figure 13: Real picture of the master and slave sections along with the open-loop control architecture.

In order to better understand how the hydraulic motor works, a sequence of CCW rotations (0° - 90° - 180° - 270° - 360°) and corresponding 'slave' piston movements, covering a full revolution of the SP, is also represented in (Figure 14), taking $S_{1/2} = 16\text{mm}$ in Eq. (2).

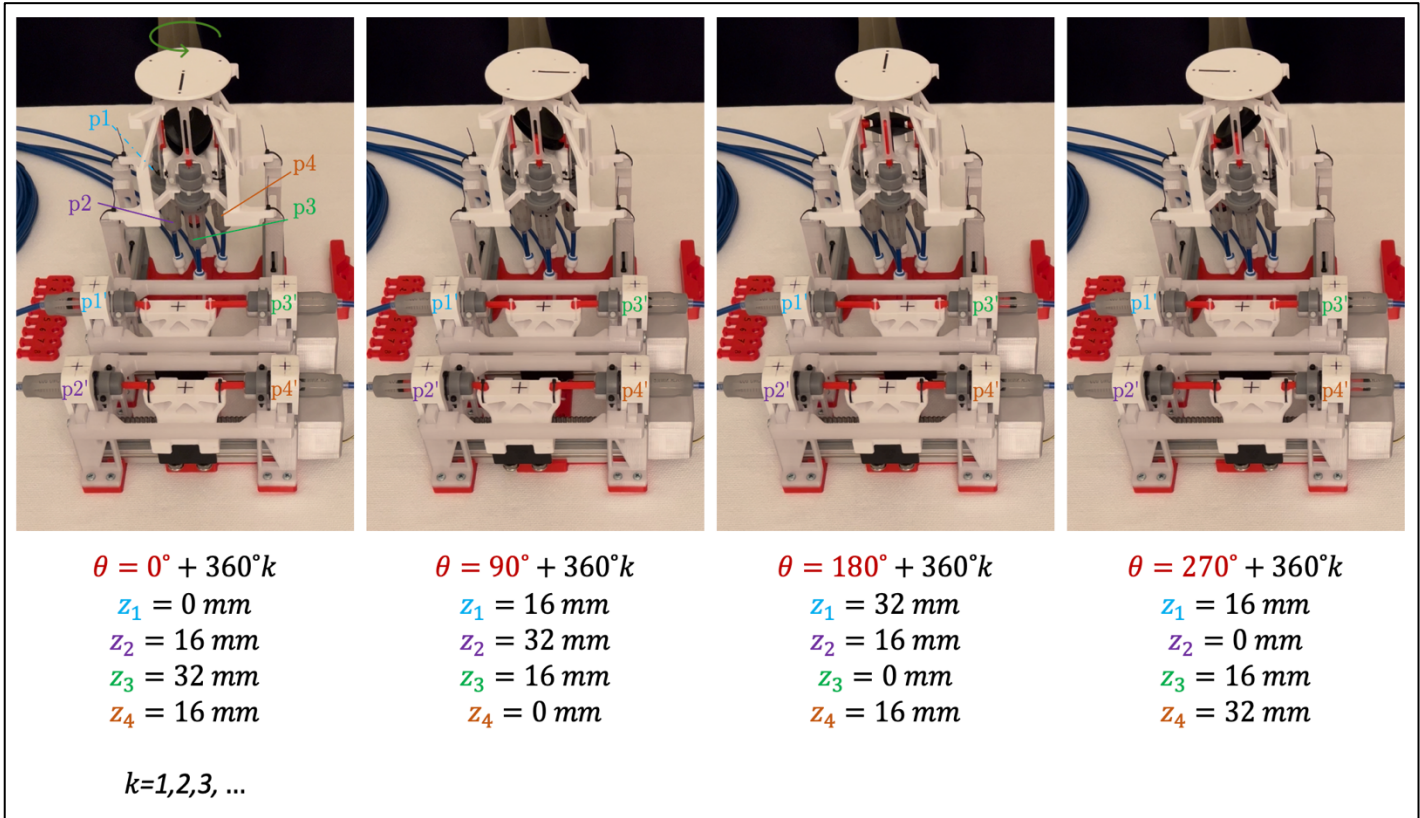


Figure 14: Sequence of CCW rotations and associated piston displacements covering a full rotation and assuming the half stroke to be 16mm.

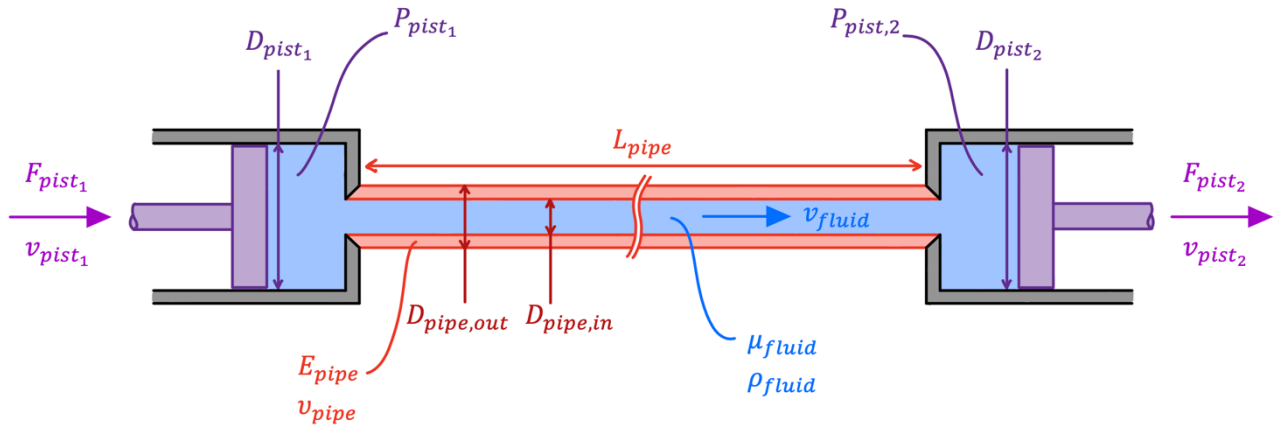
It should be noted that there is an inherent phase difference of 180° between each 'slave' piston (p1-p2-p3-p4) and its corresponding 'master' piston (p1'-p2'-p3'-p4'), making the displacements of p1', p2', p3', and p4' respectively equal to z_3 , z_4 , z_1 , and z_2 , which are the conversions used for the open-loop control from the master section.

3.2. Fluid Dynamics of the Hydraulic Transmission: Governing Equation

The overarching aim for any fluid transmission is **transparency** (Lawrence, 1993). Essentially, a transmission is defined as transparent if it perfectly transmits force, energy, and motion from the actuation source, here the master section, to the receiver, here the slave section. In order to achieve transparency, the transmission, in theory, should exhibit *no delay*, *zero damping and inertia*, and *infinite stiffness*. This offers a framework for designing and optimising the hydraulic transmission that connects the master and

slave units, where stiffness should be maximised while damping and inertia should be minimised.

To establish connections between key design parameters and the robot's performance, Figure 15, which represents a single two-piston fluid line along with the main dynamics parameters associated with the system, will be examined.



Where:

D_{pist_1}/D_{pist_2} : diameter of the piston from the master side (the 'master piston')/from the slave side

F_{pist_1} : input force, from the master section

F_{pist_2} : output force, at the slave section

v_{pist_1}/v_{pist_2} : fluid velocity at the input piston/output piston

P_{pist_1}/P_{pist_2} : fluid pressure at the input piston/output piston

E_{pipe} : pipe's modulus of elasticity (assuming the pipe is made of isotropic material)

v_{pipe} : pipe's Poisson's ratio

$D_{pipe,out}/D_{pipe,in}$: pipe's outer diameter/inner diameter

L_{pipe} : pipe's length

μ_{fluid} : fluid's dynamic viscosity

ρ_{fluid} : fluid's density

v_{fluid} : fluid's velocity

Figure 15: Schematic of a single two-piston fluid line with the associated main dynamics parameters.

The following derivations have been adapted from Buerger (2005) (Massachusetts Institute of Technology):

3.2.1. Equivalent Transmission Stiffness:

The transmission stiffness K_{equ} is considered the result of both the fluid stiffness due to compression K_{fluid} and the pipeline stiffness K_{pipe} due to the pipe's elasticity, modelled in series.

Using Lame's Equations, K_{pipe} can be found to be approximately equal to:

$$K_{pipe} = \frac{\pi E_{pipe} D_{pist_1}^4}{8L_{pipe} D_{pipe,in}^2} \left(\frac{D_{pipe,out}^2 - D_{pipe,in}^2}{D_{pipe,in}^2 + D_{pipe,out}^2 + v_{pipe} D_{pipe,out}^2 - v_{pipe} D_{pipe,in}^2} \right)$$

K_{fluid} can also be approximated as:

$$K_{fluid} = \frac{E_v A_{pist_1}^2}{V}$$

Where E_v is the fluid's bulk modulus, $A_{pist_1} = \frac{\pi}{4} D_{pist_1}^2$ is the master piston's area, and V is the total volume of fluid contained within the pipeline.

The equivalent transmission stiffness K_{equ} therefore becomes: $K_{equ} = \frac{K_{pipe} K_{fluid}}{K_{pipe} + K_{fluid}}$

3.2.2. System Damping:

The damping, assuming the flow is laminar during operation, is found to be equal to:

$$B_{fluid,laminar} = \frac{F_{pist_1}}{v_{pist_1}} = 8\pi\mu_{fluid}L_{pipe} \left(\frac{D_{pist_1}}{D_{pipe,in}} \right)^4$$

3.2.3. Fluid Inertia

The fluid inertia can be easily found through an energy calculation approach and is defined as follows:

$$m_{fluid} = m_{cylinder} + m_{pipe,in} \cdot \left(\frac{D_{pist_1}}{D_{pipe,in}} \right)^4$$

Where $m_{cylinder}$ is the equivalent mass of fluid in the cylinder and $m_{pipe,in}$ is the mass of fluid in the pipeline.

3.3. Design Trade-offs and Selection Process

Following section 3.2., it is evident that the ratio $\frac{D_{pist_1}}{D_{pipe,in}}$ has a significant impact on the dynamics of the system (e.g., laminar damping is proportional to the ratio $\frac{D_{pist_1}}{D_{pipe,in}}$ to the fourth power), especially when compared to the other parameters. For instance, this means that making the line smaller while keeping D_{pist_1} constant considerably increases damping, fluid inertia, and line stiffness. However, for the transmission to be transparent, only increasing stiffness is desirable.

One of the parameters, E_{pipe} , only affects the stiffness which means that the higher its value, the better the transmission's performance. However, this is limited by the available pipe materials as well as the operational conditions. A pipe with an extremely high E_{pipe} would be too stiff to bend, making it challenging to implement in an operation room through the master-slave configuration where a more flexible pipe would be needed. On another hand, smaller pipelines (L_{pipe}) are desirable, increasing stiffness while decreasing both damping and fluid inertia. However, these pipelines must also be long enough to connect master and slave sections, which imposes certain constraints.

For operations requiring fast response times and high positional accuracy such as catheterisation interventions, increasing stiffness is considered the most important (Dong *et al.*, 2019).

With the above-mentioned considerations in mind, the following parameters were chosen for the hydraulic transmission:

- Water is chosen as the transmission medium due to its availability and relative safety in medical conditions (with the potential to implement sterile medical-grade water).
- 7-metre long, semi-rigid nylon (PA6) tubes with inner/outer diameters of 4mm/ 6mm were chosen as the pipeline. The latter offers enough length to properly distance the master section from the MRI and provides a good trade-off between stiffness and pliability.
- For its simplicity, affordability, and ease of implementation when compared to RDs, traditional O-ring-sealed syringes with a 16.5mm cylinder inner diameter (equivalent to the piston diameter in this case) have been chosen for the first prototype.
- With the intention of implementing RDs in the future for potential friction reduction, the 3D model was designed around typical RD parameters. Therefore, a stroke of 32mm (i.e., $S_{1/2} = 16\text{mm}$ in Eq. (2)) was selected when designing the custom-made pistons, matching commercially available RD strokes.

3.4. Fabrication and Further Design Considerations

To ensure MRI compatibility, all parts of the slave section were rapidly prototyped using 3D-printed plastic materials. These were produced using both the Ultimaker S5 FDM (Fused Deposition Modelling) and the Form3 SLA (Stereolithography) printers.

Different materials were chosen based on their specific properties and the requirements of the parts they were used to create. For instance, Polylactic Acid (PLA) was selected for the pistons due to its excellent surface finish, which helps to minimise friction.

The swash plate, which must resist the pistons' 'pushing' forces without breaking or deforming, was printed from Acrylonitrile Butadiene Styrene (ABS). This material was chosen for its high impact-resistance, strength, and toughness, all while remaining lightweight.

The motor's assembly skeleton was made from Polyethylene Terephthalate Glycol (PETG), a material known for its strength and easy printability.

Lastly, Formlabs 'Grey Pro' resin, renowned for its high toughness, was used to print highly detailed cylinder housings. These are formed in two parts, joined together with a threaded bezel ring. This design is intended for future RDs implementation, where the RDs need to be securely fixed in place and compressed at their edges to provide sealing.

All other components of the slave section were also meticulously selected to ensure MRI compatibility, from the plastic nuts and bolts used to secure the cylinders in place, to the plastic glass-ball bearings affixed to the swash plate shaft and which provide frictionless rotation and maintain the shaft's position axially.

3.5. Catheter Axial Motion Unit

Finally, a catheter axial motion unit was prototyped (Figure 16).

While referring to the figure:

1. Bevel gears are connected to the Motor and drive the rollers.
2. Driving rollers (like CorpPath GRX) with a particular shape to keep the catheter in place: an additional slot is made to accommodate for typical cardiac catheter sizes of at least 1mm in diameter.

3. Sliding component with free rollers to clamp the catheter in place with rubber bands.

4. Perforated ridges on the rollers' surface to prevent slipping of the catheter.

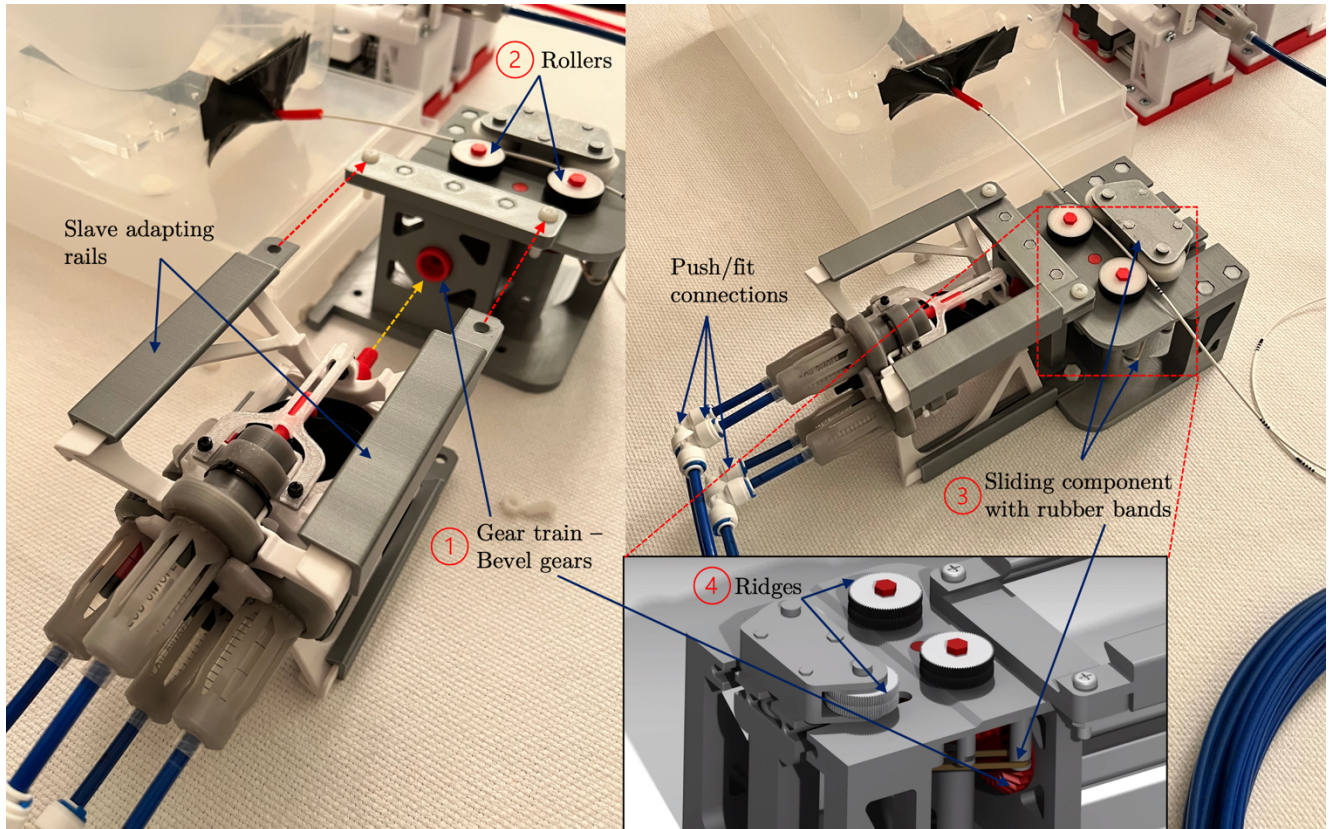


Figure 16: Catheter Axial Motion Unit Prototype.

4. Experiments, Results, and Discussions

The subsequent sections delve into the experimental evaluation of the novel design introduced earlier. Initially, the focus is on testing the hydraulic motor, specifically measuring its rotational accuracy. This is followed by an assessment of the motor when incorporated into the catheter translation unit, to evaluate its performance in the context of its intended application.

4.1. Experimental Setups

4.1.1. Hydraulic Motor Rotation Setup

Figure 19 depicts the setup of the motor rotation experiment. A circular plate measuring 10cm in diameter is affixed to the motor shaft, oriented vertically to enable data collection throughout the experiments (Figure 18). Four 2.5mm diameter circles are labelled on the surface of the disc, representing the landmarks that will be monitored. The first landmark is located at the centre of the plate, with the other three being

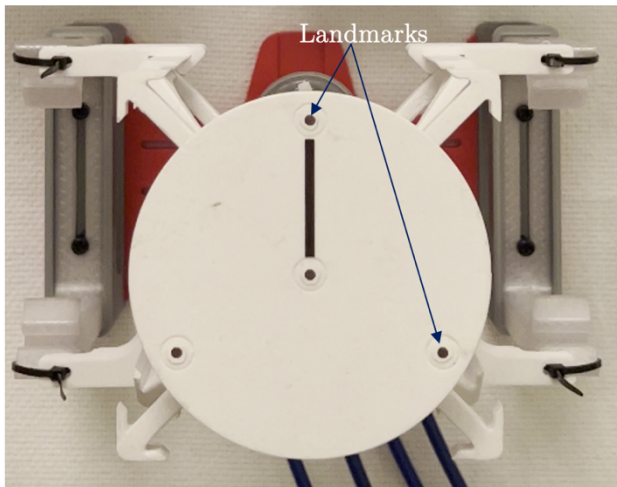


Figure 17: Vertical shot of the disk and the four circular landmarks.

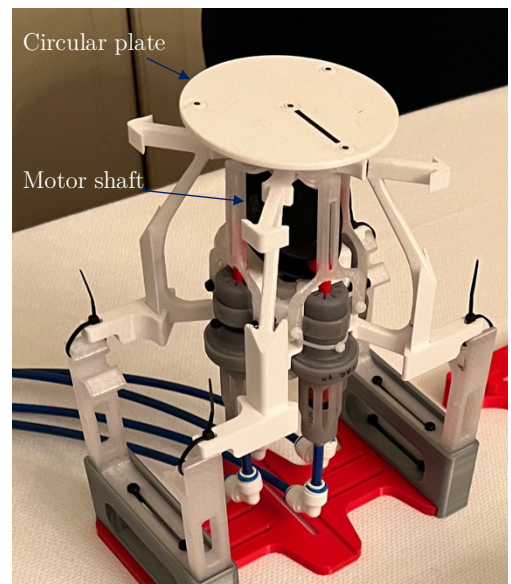


Figure 18: Close-up of the motor and the disk positioned vertically.

radially placed at 120° intervals (Figure 17) to enhance the reliability of the results in the tracking process by taking their average in terms of recorded angular displacement.

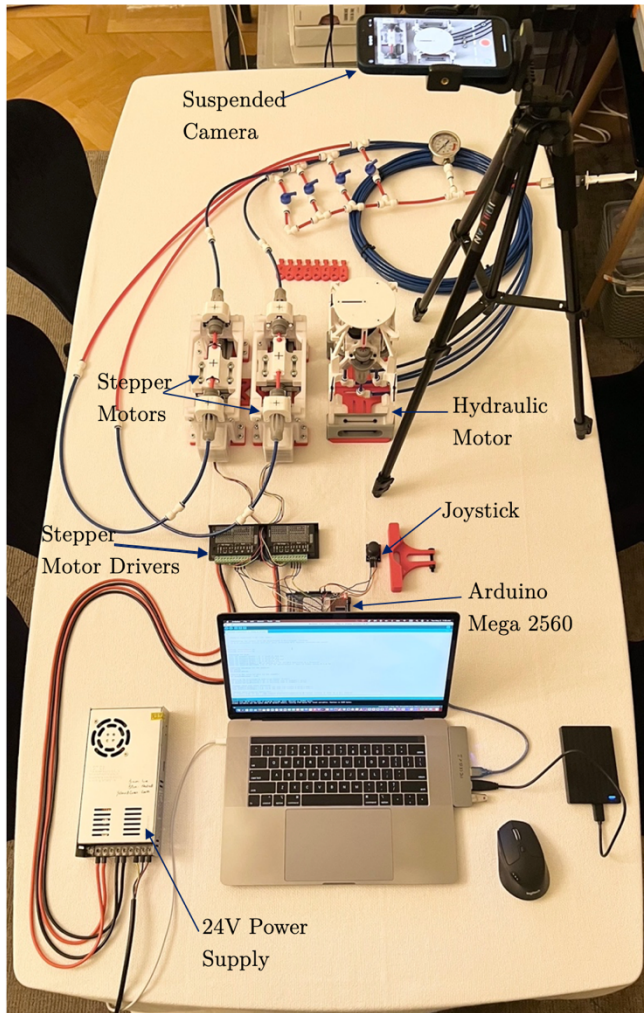


Figure 19: Hydraulic motor rotation experiment setup.

4.1.2. Catheter Translation and Cardiac Phantom Assembly

Figure 20 depicts the catheter translation experiment setup with its cardiac phantom. The motor is positioned horizontally and integrated into the catheter's axial motion unit. On the latter, four rollers of uniform size are adapted to secure the catheter in place, restricting it to axial motion. The catheter is marked with black dashes used to be tracked before reaching the aortic artery phantom. This is done to account for the bending that potentially occurs once the catheter enters the phantom as shown in Figure

21. The setup also comprises a straight segment of the aorta, which was 3D-printed with Poly-Lactic Acid (PLA), and submerged in water to emulate in-vivo cardiovascular conditions. Moreover, a 5mm acrylic plate is placed on top of the phantom to contain the catheter and serve as a viewing window.

It should be noted that in both experiments, the setups are placed next to the master section to enable simultaneous detection of the piston movements which indicates the true start and end of the experiments.

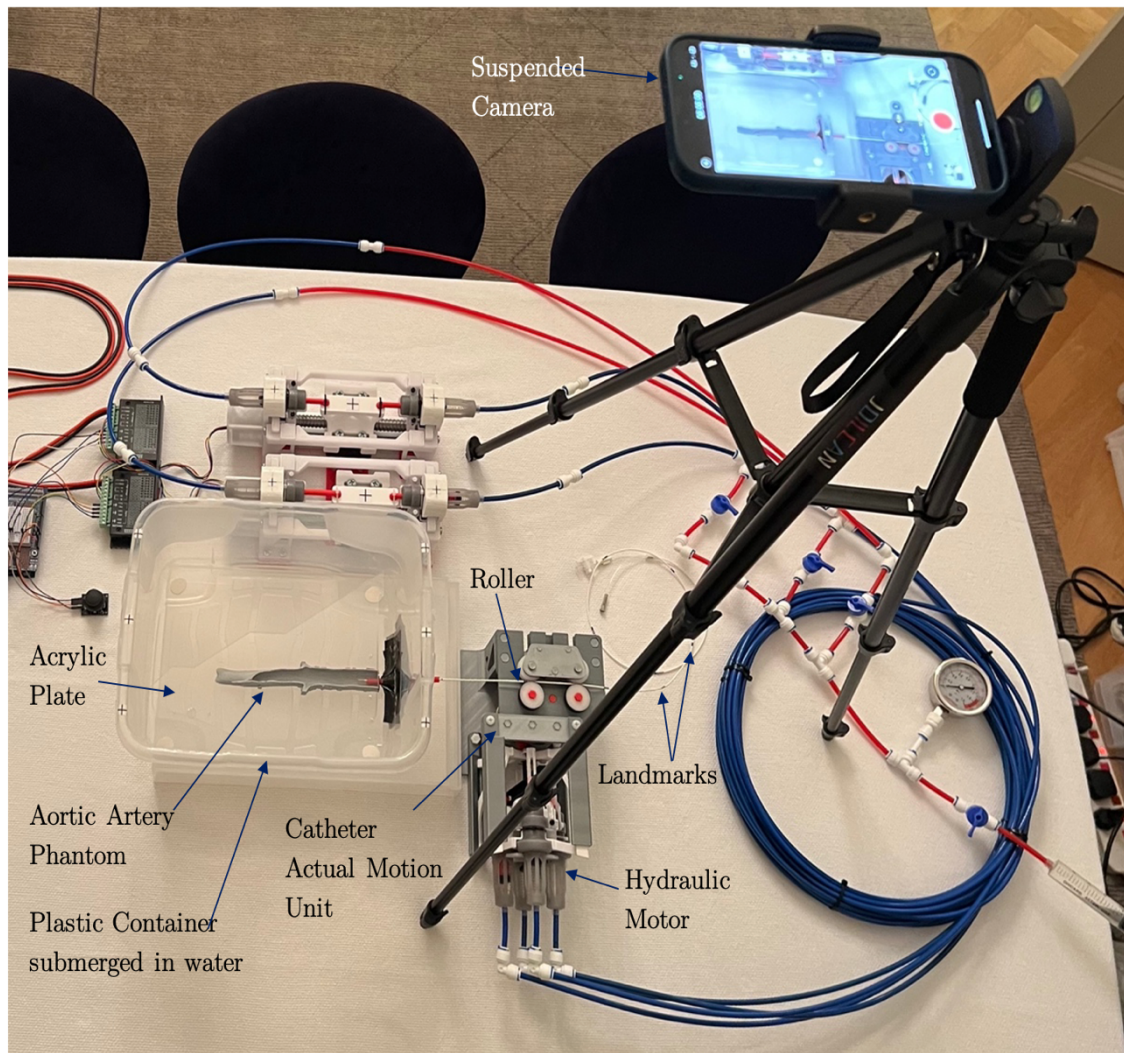


Figure 20: Catheter translation experiment setup.

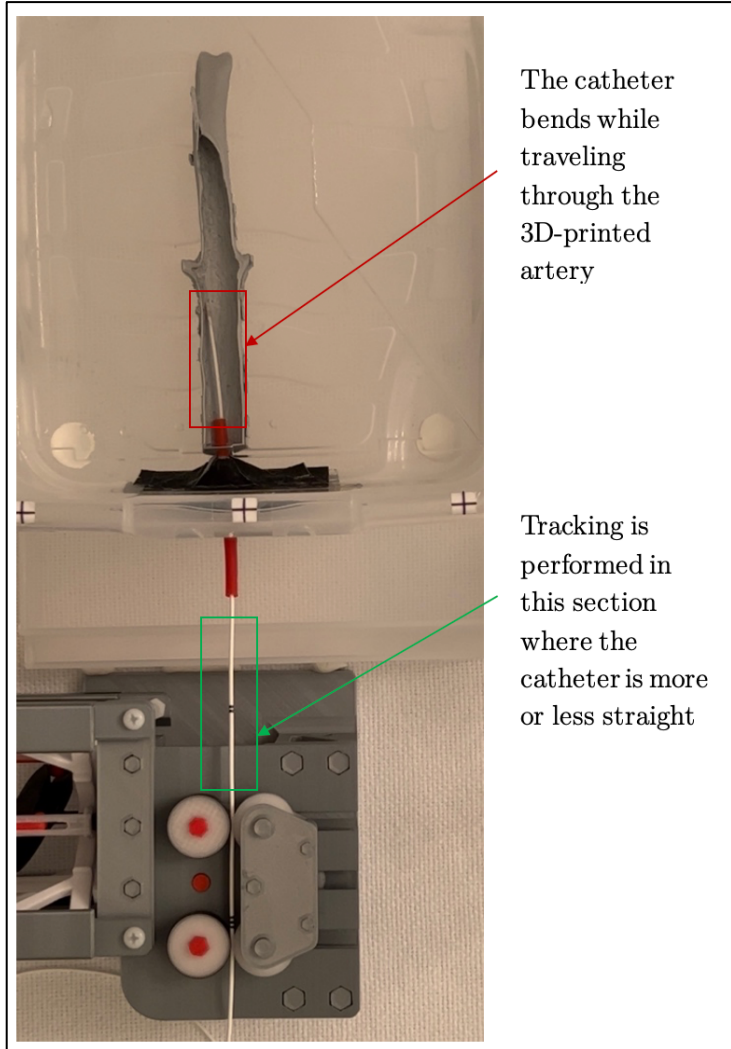


Figure 21: Tracking landmarks for the catheter translation experiment.

4.2. Measuring Performance: Data Collection & Processing

4.2.1. Positional Accuracy Experiments

The positional accuracy approach applies a predefined series of motions to the master unit which is then translated to the hydraulic motor. The aim is to monitor the final position of the slave unit at the end of each patterned sequence and compare it against its expected position. The angular and travel positions of the landmarks are determined using a measurement application named “Ruler”, that maintains an always-on-top position of a ruler and protractor on the computer screen. An example of positional data retrieval for both angular and distance positions is shown in Figure 22. Unlike angles,

distance measurements are dependent on a base measurement (pixels) and required conversion to transform them to their actual values in millimetres.

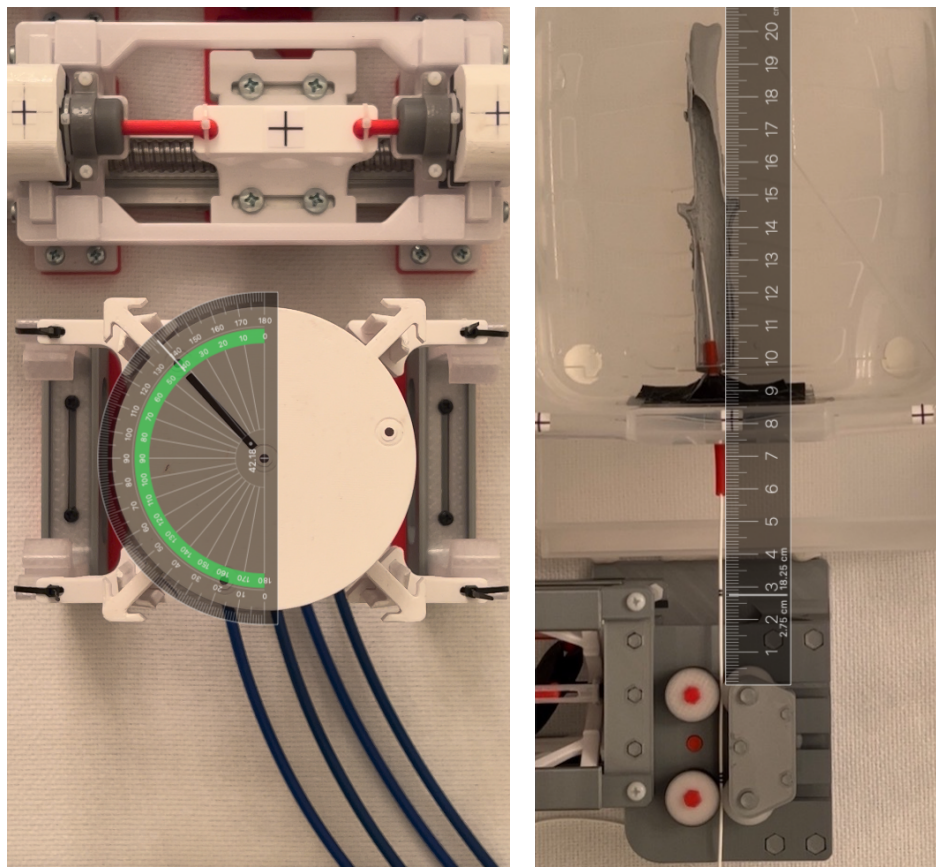


Figure 22: Example of positional data retrieval using the 'Ruler' measurement application.

4.2.2. Continuous Tracking Experiments

The continuous tracking experiments differ from the positional accuracy experiments by virtue of the landmarks being continuously tracked and monitored, allowing the measurement of positional errors at every point in time. To achieve efficient tracking, an algorithm was developed in Python 3.8 with the aid of the OpenCV 4.7.0.72 package to process pre-recorded videos of the experiments (Rosebrock, 2018). A camera is placed directly on top of the experimental setup (Figure 19-Figure 20) at a fixed distance to reduce variability in the stored data. The video capture rate is set at 30 frames per

second to balance the need for high temporal resolution and the computational cost of processing high frame rates.

The tracker used is CSRT (Channel and Spatial Reliability Tracker), a robust and high-performance tracker, recognised for its superior accuracy and reliability (Dardagan *et al.*, 2021). The tracking algorithm was designed to enable users to manually define the landmarks by encapsulating them in boundary boxes at the beginning of each experiment (Figure 24). The coordinates of the centre of each boundary box are collected and stored in a CSV (Comma Separated Values) file. Figure 23 presents the tracking algorithm flowchart.

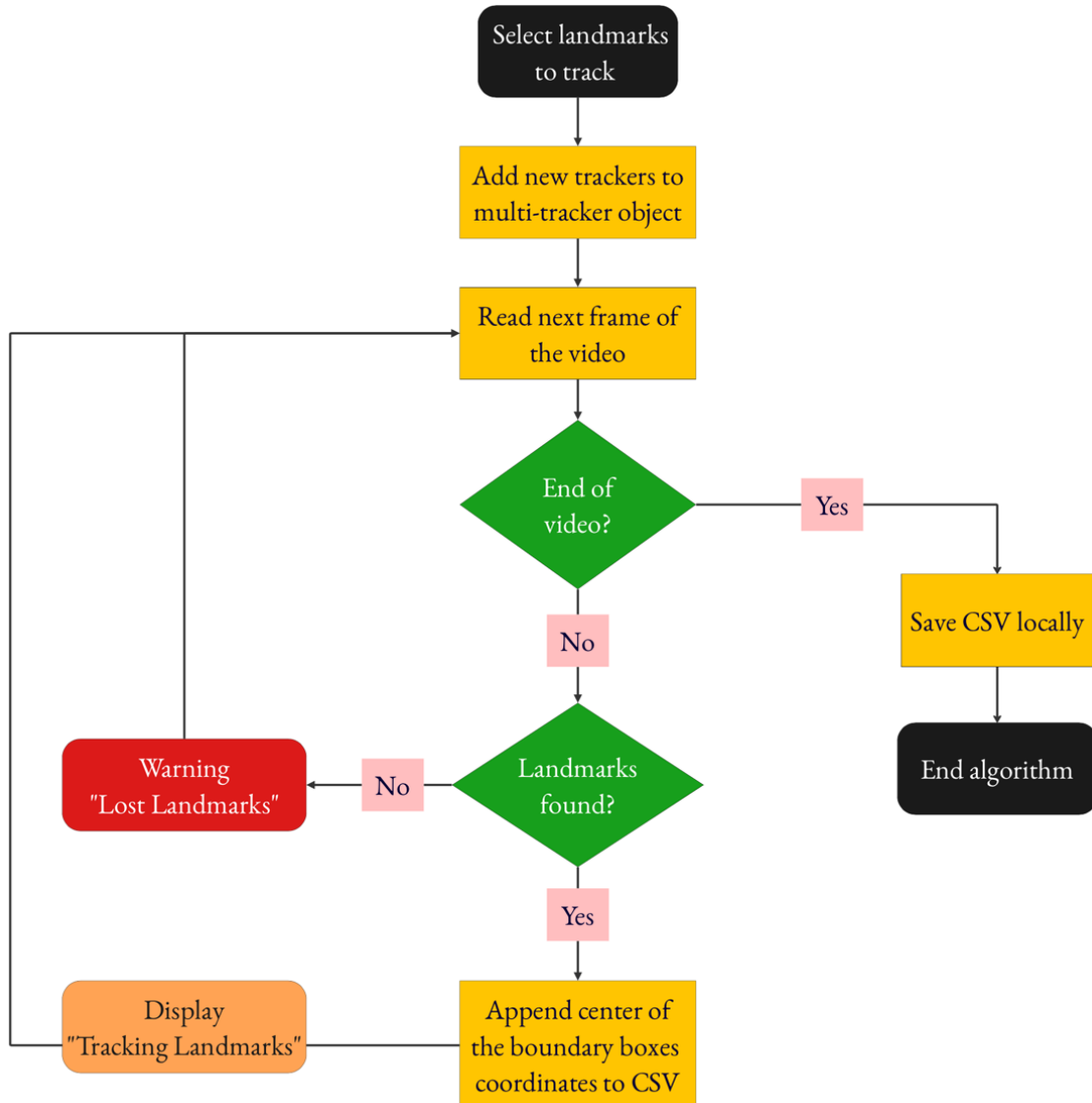


Figure 23: Tracking algorithm flowchart.

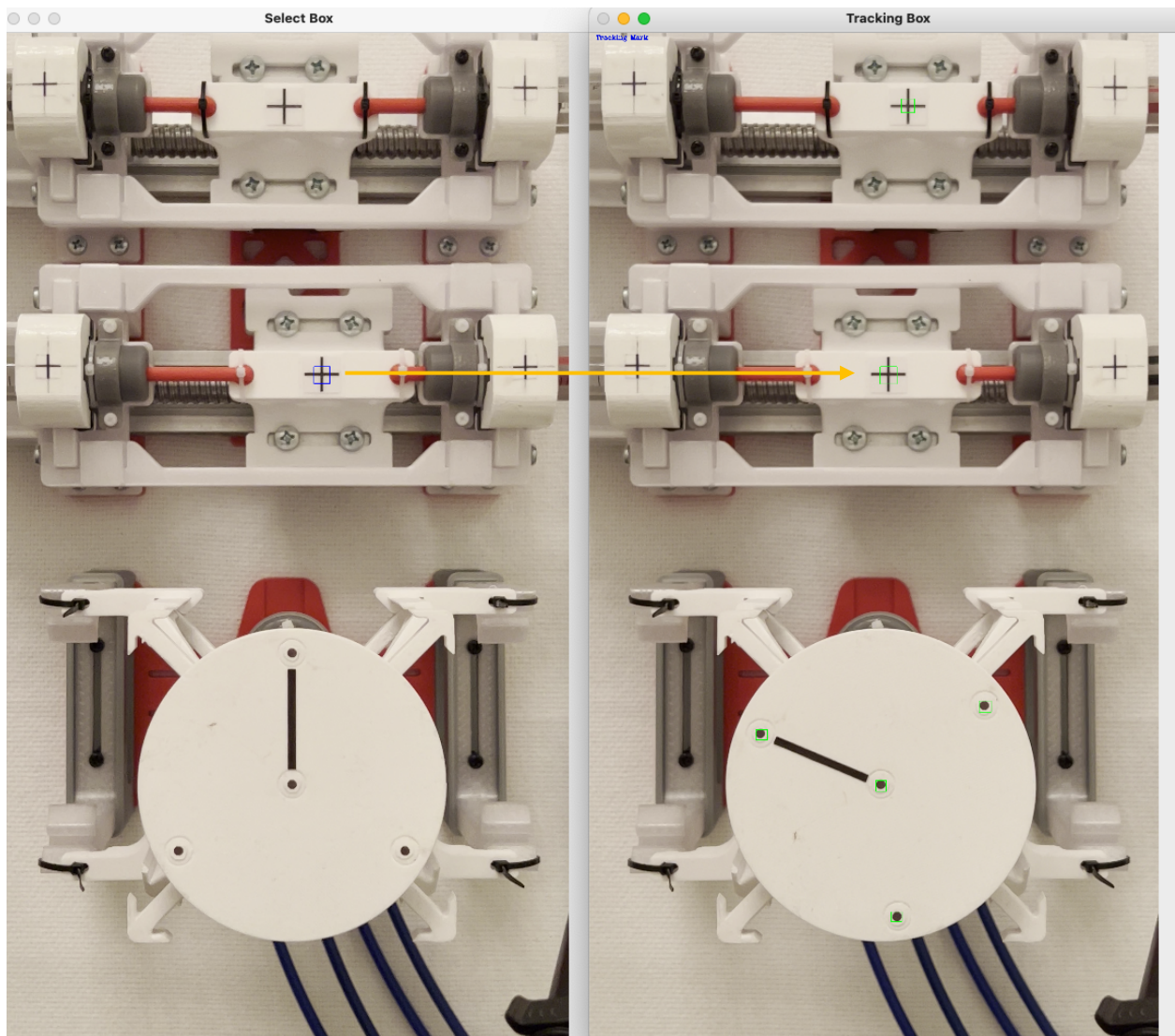


Figure 24: Example of boundary box encapsulation for landmark monitoring during manual selection (left; blue box) and monitoring (right; green boxes).

4.2.3. Experimental Metrics

To ensure reliability when analysing data with experimental metrics, it is effective and recommended to conduct at least five repeats of each experiment (Li *et al.*, 2012). This allows for the identification of outliers or anomalies in the data and ensures that the results are consistent across multiple trials. All of the experiments conducted in this study were repeated **ten times each**.

One efficient method for assessing the degree to which a data set is spread around its mean value is by utilising the standard deviation σ .

Standard Deviation (SD):

$$\sigma = \sqrt{\frac{1}{(n-1)} \sum_{i=1}^n (x_i - \bar{x})^2}$$

The individual values of the dataset and their mean are represented by x_i and \bar{x} respectively, where n denotes the size of the dataset (King and Eckersley, 2019).

4.3. Experiment (A): Hydraulic Motor Rotation: *Positional Accuracy*

Experiment (A) consists of manually measuring the motor's angular displacement θ_a by comparing it against the expected input angle θ_e controlled by the master section. The error between the actual and expected angles, $\Delta\theta = \theta_e - \theta_a$, is then calculated. This error is computed for each of the input angles from 45° to 360° in 45° angle increments, and repeated for each iteration of the experiment. All the errors are displayed along with their associated mean and SD.

The motor always restarts from 0° to execute any of the angular inputs within the defined sequence. The observed errors are consistently positive, with an average error of 2.484° and a range spanning from 0.9° to 3.68° (Figure 25). Large errors were observed between the 45 - 90° segment, with a decrease of up to 1.5° in the 135 °- 225° segment before increasing again for the last three inputs. The standard deviation remained relatively stable across all input angles, with a lower variation observed in the 135 °- 225° segment.

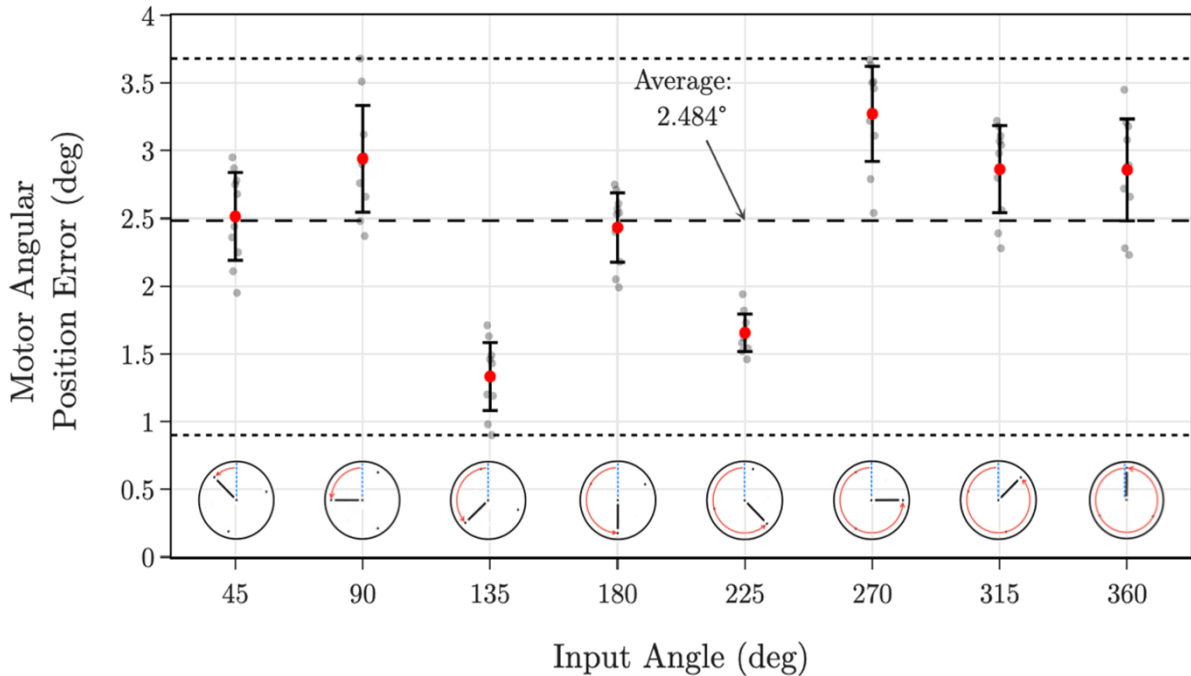


Figure 25: Plot of the mean and SD of the motor's angular position error recorded for different input angles as shown by the disk schematics. An average error of 2.484° was recorded.

4.4. Experiment (B): Hydraulic Motor Rotation: *Continuous Tracking*

In experiment (B), continuous tracking of the motor's angular position is performed and compared to the corresponding input angle, which describes a motion with a constant angular velocity of approximately $14^{\circ}/\text{s}$. The continuous cyclic motion commences at 0° , then proceeds with two sequential counter-clockwise (CCW) rotations totalling 720° , before returning to the starting position by clockwise (CW) rotation after a 3-second pause. Figure 26 displays the absolute error which averages at 1.803° , ranging from 0.3° to 3.25° , with the output angle stalling at 1.9° below the input angle during the pause. A consistent lag between the motor's output and corresponding input angles can be observed, with the master angle continuously leading the motion. The absolute angle difference indicates that the error exhibits periodic and repeated patterns throughout the experiment.

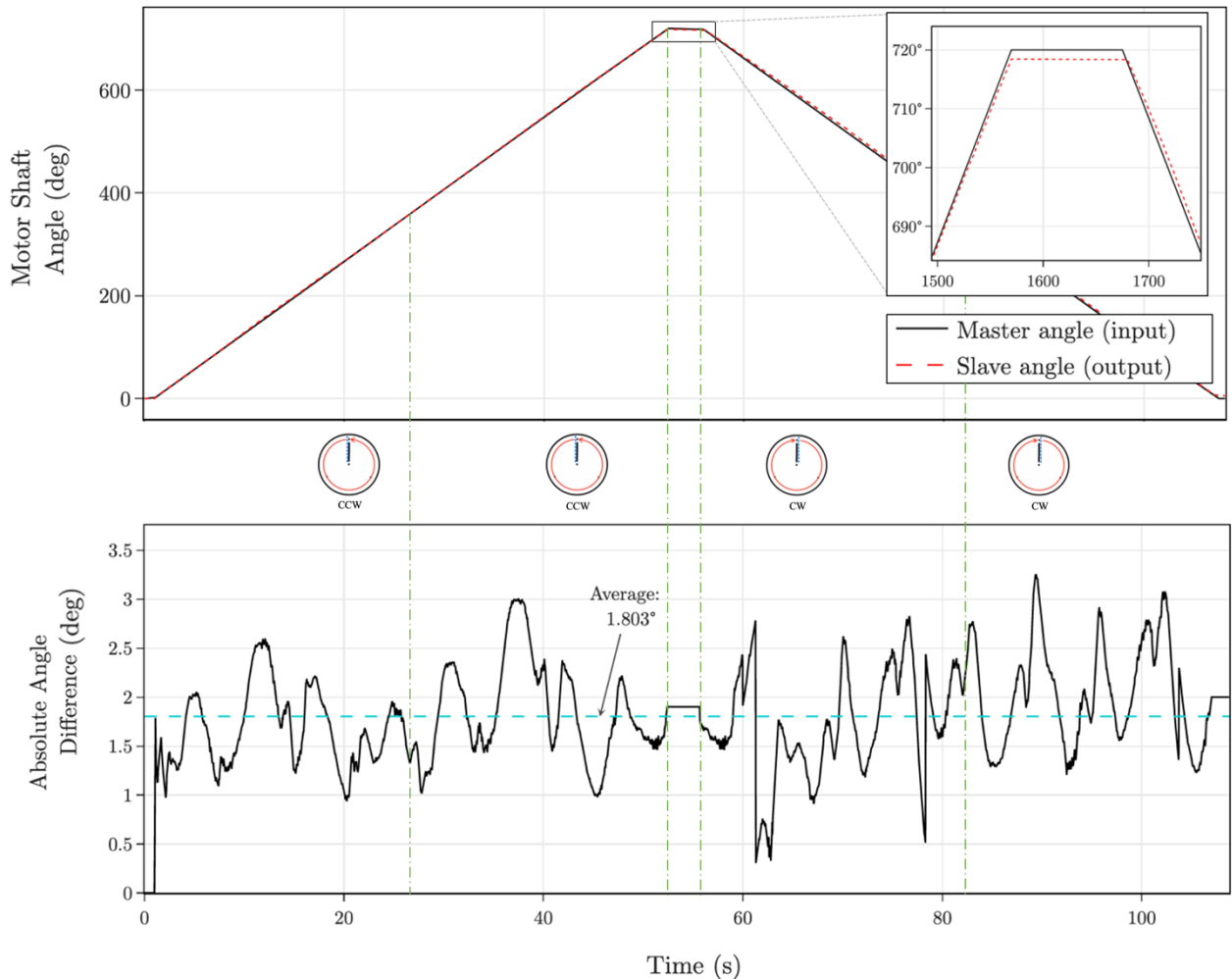


Figure 26: Continuous tracking of the motor's angular position through CCW and CW revolutions as shown by the disk schematics. An average error of 1.803° was recorded between input and output.

4.5. Experiments (C): Catheter Translation

4.5.1. Experiment (C.1): Axial Motion: *Positional Accuracy*

In experiment (C.1), the absolute positional error for catheter translation is calculated similarly to the positional error in experiment (A). Starting from 0mm, the input for catheter translation dictates sequential insertions by 10-20-30-40-10 mm. This is followed by two extractions of 50mm then 60mm, and ends with one 100mm round trip inside the aorta. Figure 27 displays the absolute positional error, with the mean calculated at 1.069mm and the range of deviation ranging from 0 to 3mm. Notably, error spikes are observed at every change of direction, before gradually diminishing and stabilizing. The

first error peak is observed at the initial insertion increment of 10mm, followed by a gradual decrease until the next peaks are observed at 110 and 60mm. Subsequently, during the catheter's return to the initial position at 0mm, the error gradually decreases before rising again to a peak at 100mm.

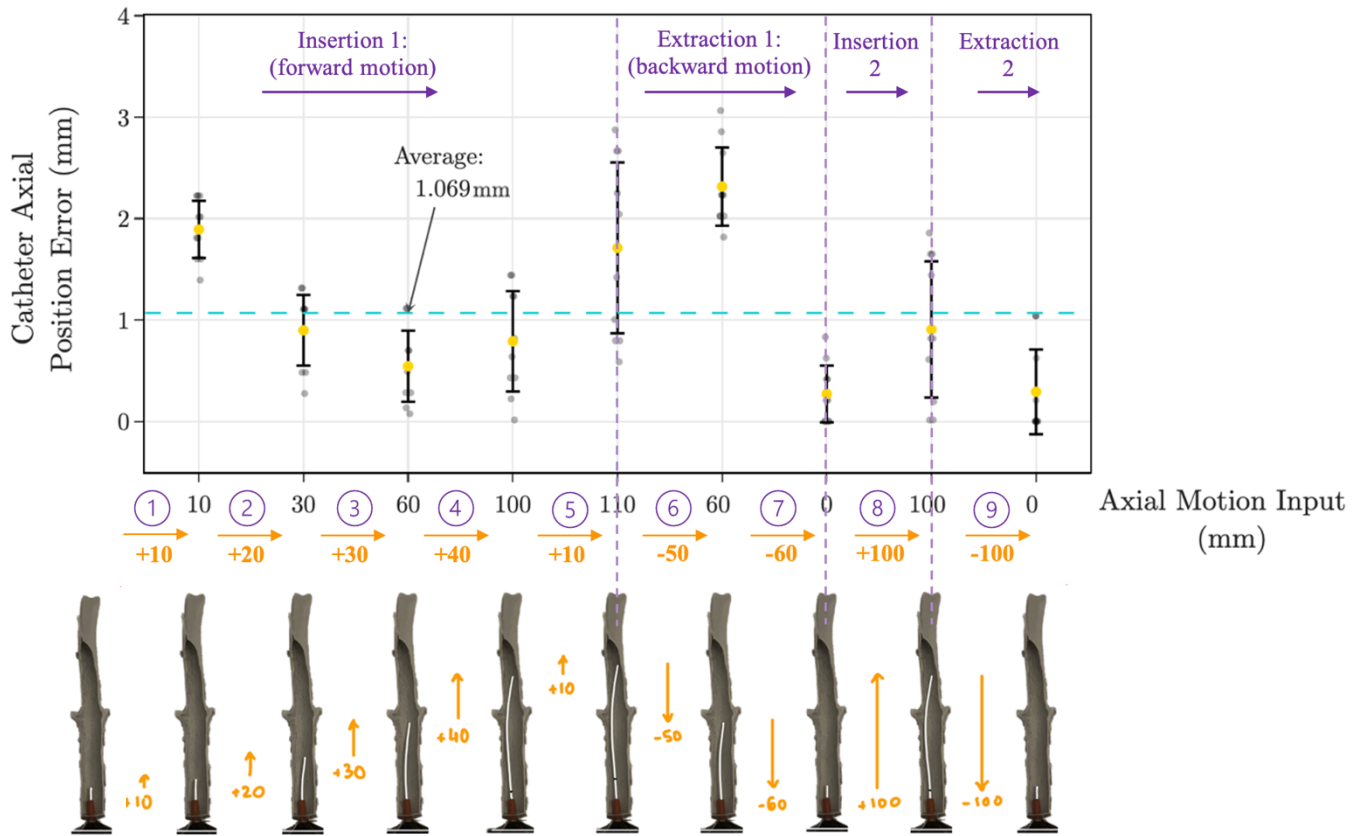


Figure 27: Plot of the mean and SD of the catheter's absolute axial position error recorded for different axial motion inputs as shown by the artery schematics. An average error of 1.069 mm was recorded.

4.5.2. Experiment (C.2): Axial Motion: *Continuous Tracking*

Figure 28 relates to the last experiment where tracking of the catheter's axial position is performed and compared to the corresponding input translation which is estimated knowing the diameter of the driving rollers. The tracking is done over the 100mm round trip characterised by a constant translational velocity of approximately 2.9mm/s. The absolute error averages 0.784mm, with the catheter position stopping at 1mm below the inputted axial motion angle during the delay, matching the mean error in (C.1). The results are also similar to the ones observed in experiment (B), where the motor's output

angle consistently lags behind its corresponding input, with the absolute angle difference exhibiting recurrent trends.

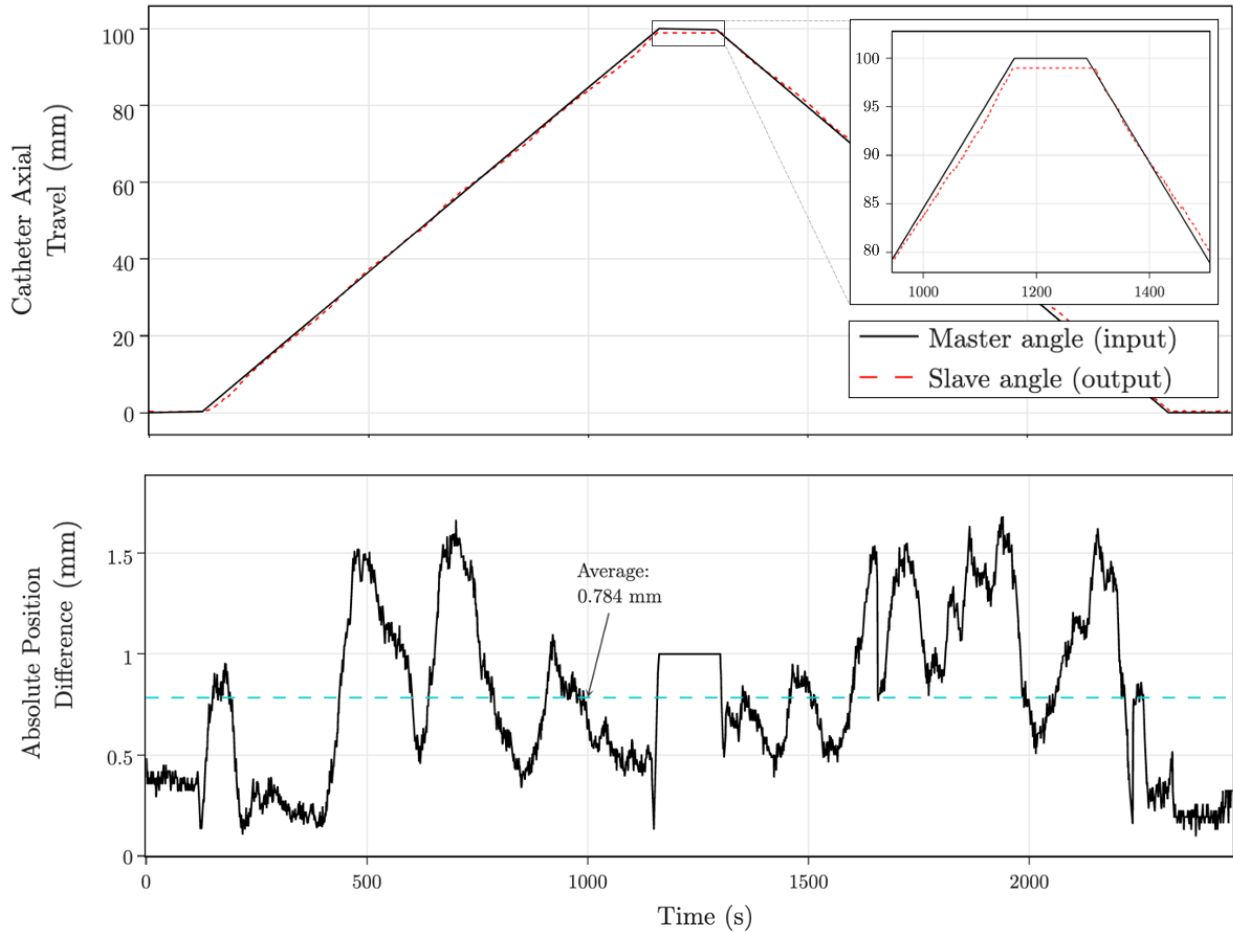


Figure 28: Continuous tracking of the catheter's axial position through a 100mm insertion and extraction. An average error of 0.784mm was recorded between input and output.

4.6. Discussions

4.6.1. Experiments (A)-(B): Hydraulic Motor Rotation

It can be seen in Figure 25 (Exp-A) that all measured errors are positive, with the same trend noticeable in Figure 26 (Exp-B), as the slave angle settles below the master angle during the pause. This observation indicates that the output angle of the hydraulic motor doesn't reach the corresponding input angle for any incremental or cyclic motion.

This can be attributed to the inherent friction in the system, which introduces non-linearities and mechanical losses that impede the smoothness of the rotation (Ellis, 2012).

The primary source of friction is the contact between the piston and the swash plate walls which move relative to each other. Additionally, the tight O-ring sealing of the piston-syringe paradigm exhibits a significant Coulomb (sliding) friction, as evidenced by the slave angle settling 1.9° below the master angle during the pause (Figure 26). It is noteworthy that during the loading of the pistons onto the swash plate configuration and associated leadscrew stepper motors linear apparatus, the Coulomb (static) friction prevented precise loading of the pistons at the desired strokes. The differences of a few fractions of a millimetre in the pistons' positions resulted in some pistons exerting more pressure against the plate by being slightly above or below the anticipated stroke. The phenomenon was most noticeable in the 45° - 90° and 270° - 360° segments (Figure 25) where errors were larger, coinciding with a swash plate rotation appearing less smooth compared to the rest. The observed recurrent patterns in the residual plots of Figure 26 further validate the imperfect loading of the pistons, which leads to varying levels of friction along different segments of the rotation, resulting in the patterned errors.

Despite attempts to minimize the gap during piston design, the rubber gasket situated at the top of the piston has a tight O-ring seal and a slight clearance at its attached position in the piston. The clearance, along with the compressibility of the gasket, indirectly impacts the positions of the piston strokes. The swash plate was also securely affixed and supported by plastic bearings (nylon cage and glass balls); however, some small axial movements were still possible due to the clearance in the ball bearings. Another factor that impacted the results is hysteresis, referring to the event where the output of a system depends not only on the current input, but also on the system's history (Tumanski, 2008). In the case of the hydraulic motor, hysteresis may arise due to the material's elasticity and friction accumulated, causing a lag in the system's response to changes in input (Figure 26).

Finally, while the data collection tools introduced provide accurate measurements, it is still subject to errors. For the positional accuracy approach, the data extracted depends on the resolution of the computer screen, and the user's manual dexterity. Additionally, the boundary boxes used to detect the markers in the continuous tracking experiments may not always encapsulate the exact location of the marker's centre and cause it to fluctuate in-between frames.

4.6.2. Experiments (C): Catheter Translation

Figure 28 observations, including the lower position during the pause and systematic errors, can be attributed to the effects of seal friction and piston loading, similar to the findings of Figure 26. Additionally, other sources of error may have influenced the catheter translation outcomes. Indeed, although the experiment was designed to enforce straight-line axial movement of the catheter, its inherent flexibility led to slight deviations from linear motion, introducing inaccuracies in the measurements. Moreover, the clearances between mated gear teeth (gear backlash) (Margielewicz, Gąska and Litak, 2019), the connection between the swash plate shaft and bevel gear, the movement of parts within the catheter axial motion unit, and roller clamping effectiveness significantly contributed to the errors. The large errors observed in Figure 27 (at 10, 60 and 100mm) can be attributed to the presence of dead band caused by the apparatus aforementioned clearances. Specifically, when the catheter's direction of travel is reversed, the clearance between mating parts creates a dead zone where no movement occurs until the clearance is eliminated (de Silva, 2002). Finally, the lack of precision observed at 110mm can be attributed to the tracker's difficulty to track the landmark with low visibility after it entered the phantom artery, as depicted in Figure 29.

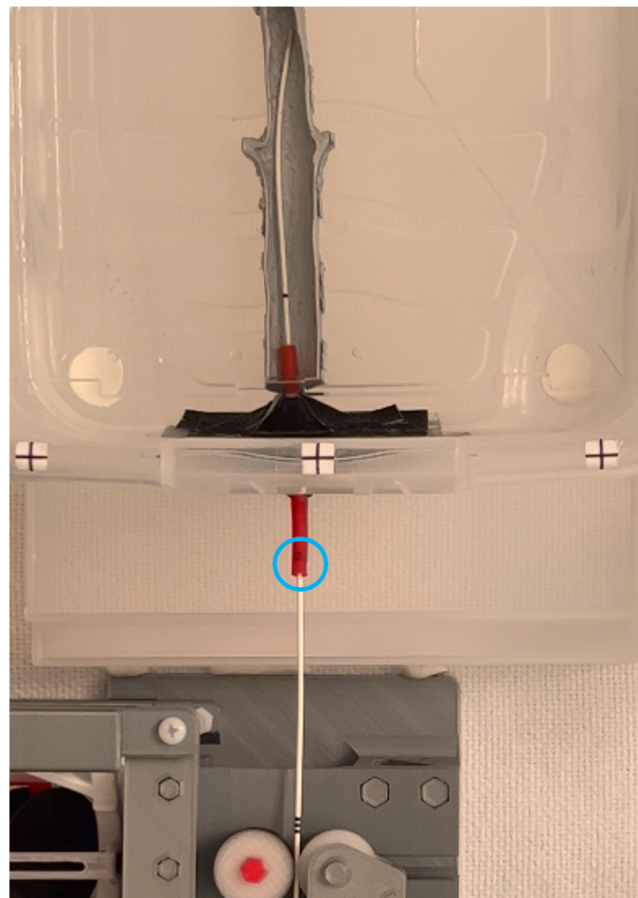


Figure 29: Landmark visibility once entering the phantom artery.

5. Conclusion

5.1. Key Results and Consequences

This study has accomplished its aim and met the targeted objectives, which encompassed the successful development of an MRI-compatible motor not only applicable for catheterisation but for all MRI-guided procedures. The presented hydraulic motor featured both precise rotation control (average error of 2.48° and 1.80° for the positional accuracy (PA) and continuous tracking (CT) experiments respectively) and enhanced axial motion of the catheter (average error of 1.07mm for PA and 0.78mm for CT).

Previous research conducted by Lee et al. (2018) explored hydraulic systems for catheterisation robotics and reported a continuous tracking error of 0.64° compared to an error range spanning from 0.3° to 3.25° in the CT experiments. Furthermore, Thakur et al. (2009) found that conventional remote catheter navigation achieved replication of axial motion within 1mm with a delay of under 300ms, which closely aligns with the outcomes of the catheter translation experiments conducted.

In summary, the results obtained showcase a promising step forward in the transition towards MRI-guided interventions and demonstrate the success of the developed system in terms of catheter translation when compared to conventional methods.

5.2. Limitations and Future Work

To further expand the capabilities of the proposed MRI-compatible catheterisation robot, future efforts will be directed towards enhancing several key aspects.

As delineated in section 4.6, the prototype's design exhibits significant backlash and friction unveiled through the recurring pattern and discrepancies observed in the error plot of the experiments. These issues can be attributed to factors such as clearances in

the apparatus, 3D-printing finishing, and O-ring coulomb friction, inherent in the prototype's design and material. To address these concerns, future iterations of the motor can incorporate a pre-conceived Rolling-Diaphragm (RD) design (Figure 31), aimed at reducing friction in O-ring rubber gaskets. Although not in the scope of this study, the whole CAD model was based on a parametric design using more than 80 RD-related parameters (Figure 30), indicating the potential for significant performance improvements.

Additionally, the dynamics study of the swash plate mechanism can establish more precise design guidelines through their dynamic optimisation with lower friction components, facilitating the selection of optimal parameters.

To enhance the characterisation of the prototype's performance, step response experiments can be conducted under an MRI by subjecting it to sudden input changes, providing insights into its responsiveness and delays. Furthermore, the force/torque transmission performance can be evaluated through a weightlifting experiment, while sinusoidal positional tracking and positional frequency response experiments can assess the system's capability to follow periodic motion patterns.

On the other hand, the tracking experiments were conducted at very low speeds, such as $14^\circ/\text{s}$ (Exp-B) and 2.9mm/s (Exp-C). This limitation primarily emanated from the type of stepper motor used, presenting a trade-off between speed and accuracy. To ensure clinical applicability that requires faster insertion/extraction rates, clinicians may potentially switch to more accurate servo motors.

Finally, the limited level of spatial resolution captured by the tracking algorithm ($\sim 54.5\text{PPM}$ (Pixels-per-Millimetre)), the 2D monitoring technique and setup employed introduced more inaccuracies. Potential solutions include the use of Bi-plane imaging with two orthogonal high-resolution cameras and additional sensors/imaging modalities that offer a more efficient way to measure catheter translation.

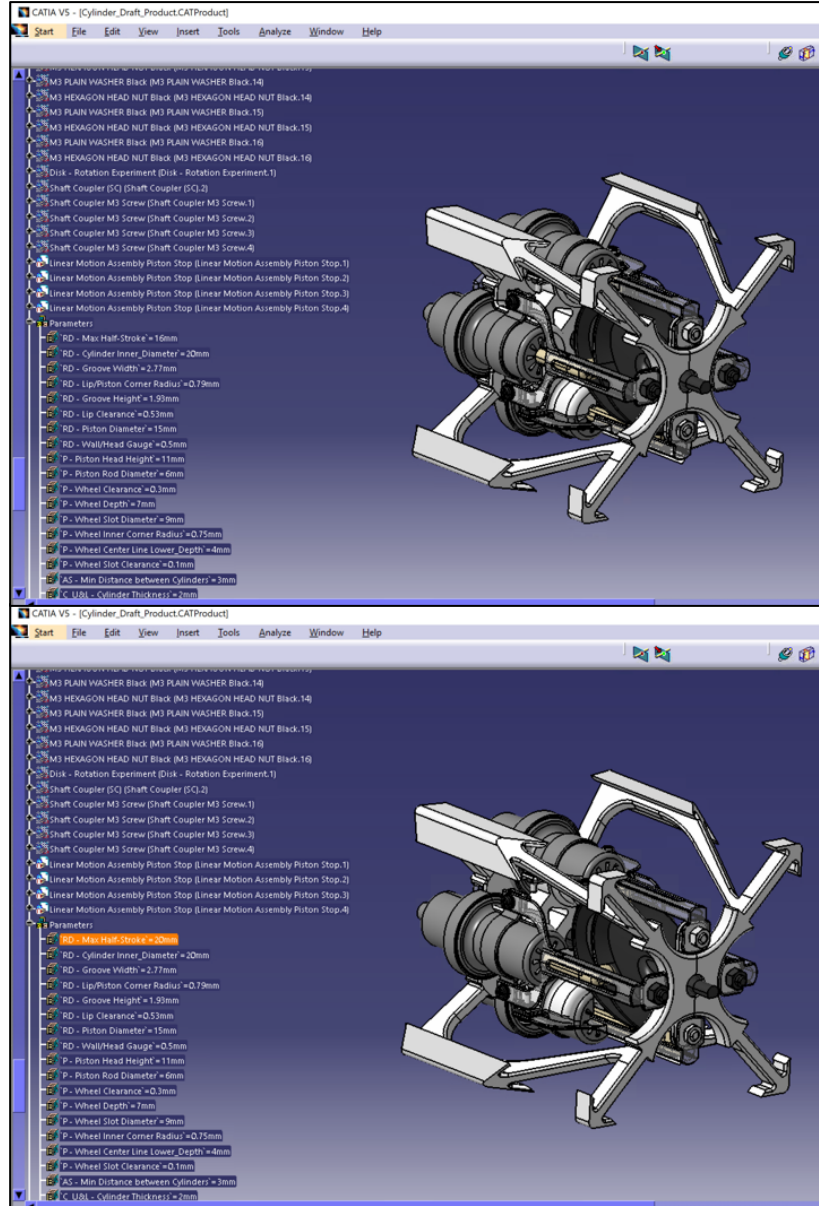


Figure 30: CATIA screenshots showing the initial model (top) vs. the updated model (bottom) where the maximum available half RD/piston stroke was increased from 16mm to 20mm, which consequently extends the length of the motor.

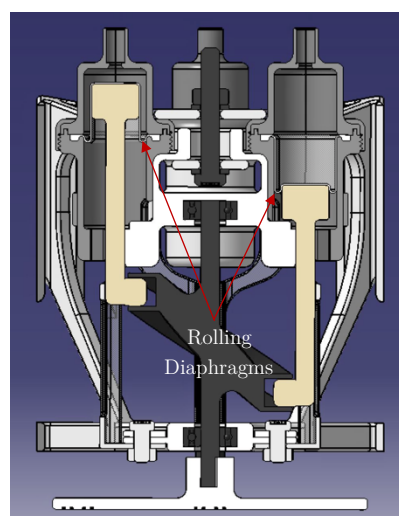


Figure 31: Cross-section of the motor with incorporated Rolling Diaphragms.

6. Bibliography

- Abdelaziz, M.E.M.K. *et al.* (2019) ‘Toward a Versatile Robotic Platform for Fluoroscopy and MRI-Guided Endovascular Interventions: A Pre-Clinical Study’, *IEEE International Conference on Intelligent Robots and Systems*, pp. 5411–5418. Available at: <https://doi.org/10.1109/IROS40897.2019.8968237>.
- Aliaga, I., Rubio, Á. and Sánchez, E. (2004) ‘Experimental Quantitative Comparison of Different Control Architectures for Master-Slave Teleoperation’, *IEEE Transactions on Control Systems Technology*, 12(1), pp. 2–11. Available at: <https://doi.org/10.1109/TCST.2003.819586>.
- Badawy, M.K. *et al.* (2016) ‘A Review of Radiation Protection Solutions for the Staff in the Cardiac Catheterisation Laboratory’, *Heart, lung & circulation*, 25(10), pp. 961–967. Available at: <https://doi.org/10.1016/J.HLC.2016.02.021>.
- Baim, D.S. (2007) ‘Grossman’s Cardiac Catheterization, Angiography, and Intervention, 7th edn (2005).’, *The Canadian Journal of Cardiology*, 23(7), p. 602. Available at: /pmc/articles/PMC2650768/ (Accessed: 7 May 2023).
- Benjamin, E.J. *et al.* (2018) ‘Heart Disease and Stroke Statistics-2018 Update: A Report From the American Heart Association’, *Circulation*, 137(12), pp. E67–E492. Available at: <https://doi.org/10.1161/CIR.0000000000000558>.
- Berczeli, M. *et al.* (2022) ‘Telerobotic Endovascular Interventions and Their Potential for Cerebrovascular Treatment’, *Texas Heart Institute Journal*, 49(2). Available at: <https://doi.org/10.14503/THIJ-21-7608>.
- Berger, A. (2002) ‘How does it work?: Magnetic resonance imaging’, *BMJ: British Medical Journal*, 324(7328), p. 35. Available at: <https://doi.org/10.1136/BMJ.324.7328.35>.
- Britz, G.W. *et al.* (2019) ‘Neuroendovascular-specific engineering modifications to the CorPath GRX Robotic System’, *Journal of neurosurgery*, 133(6), pp. 1830–1836. Available at: <https://doi.org/10.3171/2019.9.JNS192113>.
- Buerger, S.P. (2005) *Stable, high-force, low-impedance robotic actuators for human-interactive machines*. Available at: <https://dspace.mit.edu/handle/1721.1/34130> (Accessed: 15 May 2023).
- Calkins, H. *et al.* (2012) ‘2012 HRS/EHRA/ECAS expert consensus statement on catheter and surgical ablation of atrial fibrillation: recommendations for patient

selection, procedural techniques, patient management and follow-up, definitions, endpoints, and research trial design: a report of the Heart Rhythm Society (HRS) Task Force on Catheter and Surgical Ablation of Atrial Fibrillation. Developed in partnership with the European Heart Rhythm Association (EHRA), a registered branch of the European Society of Cardiology (ES', *Heart rhythm*, 9(4), pp. 632-696.e21. Available at: <https://doi.org/10.1016/J.HRTHM.2011.12.016>.

Cardiovascular diseases (CVDs) (2021) *World Health Organization / WHO*. Available at: [https://www.who.int/news-room/fact-sheets/detail/cardiovascular-diseases-\(cvds\)](https://www.who.int/news-room/fact-sheets/detail/cardiovascular-diseases-(cvds)) (Accessed: 7 May 2023).

Carvalho, P.A.W.G. *et al.* (2020) 'Demonstration and Experimental Validation of Plastic-Encased Resonant Ultrasonic Piezoelectric Actuator for Magnetic Resonance Imaging-Guided Surgical Robots', *Journal of engineering and science in medical diagnostics and therapy*, 3(1). Available at: <https://doi.org/10.1115/1.4044609>.

Chakravartti, J. and Rao, S. V. (2019) 'Robotic assisted percutaneous coronary intervention: Hype or hope?', *Journal of the American Heart Association*, 8(13), p. 12743. Available at: <https://doi.org/10.1161/JAHA.119.012743>.

Chambers, C.E. *et al.* (2011) 'Radiation safety program for the cardiac catheterization laboratory', *Catheterization and Cardiovascular Interventions*, 77(4), pp. 546–556. Available at: <https://doi.org/10.1002/CCD.22867>.

Cruddas, L., Martin, G. and Riga, C. (2021) 'Robotic endovascular surgery: current and future practice', *Seminars in vascular surgery*, 34(4), pp. 233–240. Available at: <https://doi.org/10.1053/J.SEMVASCSURG.2021.10.002>.

Dardagan, N. *et al.* (2021) 'Multiple Object Trackers in OpenCV: A Benchmark', *IEEE International Symposium on Industrial Electronics*, 2021-June. Available at: <https://doi.org/10.1109/ISIE45552.2021.9576367>.

Dong, Z. *et al.* (2019) 'High-Performance Continuous Hydraulic Motor for MR Safe Robotic Teleoperation', *IEEE Robotics and Automation Letters*, 4(2), pp. 1964–1971. Available at: <https://doi.org/10.1109/LRA.2019.2899189>.

Dong, Z. *et al.* (2022) 'Shape Tracking and Feedback Control of Cardiac Catheter Using MRI-Guided Robotic Platform-Validation With Pulmonary Vein Isolation Simulator in MRI', *IEEE Transactions on Robotics*, 38(5), pp. 2781–2798. Available at: <https://doi.org/10.1109/TRO.2022.3154691>.

Ellis, G. (2012) 'Nonlinear Behavior and Time Variation', *Control System Design Guide*, pp. 235–260. Available at: <https://doi.org/10.1016/B978-0-12-385920-4.00012-6>.

Feng, Z.Q. *et al.* (2015) ‘Design and evaluation of a bio-inspired robotic hand for percutaneous coronary intervention’, *Proceedings - IEEE International Conference on Robotics and Automation*, 2015-June(June), pp. 5338–5343. Available at: <https://doi.org/10.1109/ICRA.2015.7139944>.

Fernández-Gutiérrez, F. *et al.* (2015) ‘Comparative ergonomic workflow and user experience analysis of MRI versus fluoroscopy-guided vascular interventions: an iliac angioplasty exemplar case study’, *International Journal of Computer Assisted Radiology and Surgery*, 10(10), pp. 1639–1650. Available at: https://www.academia.edu/57513870/Comparative_ergonomic_workflow_and_user_experience_analysis_of_MRI_versus_fluoroscopy_guided_vascular_interventions_a_n_iliac_angioplasty_exemplar_case_study (Accessed: 8 May 2023).

Fihn, S.D. *et al.* (2014) ‘2014 ACC/AHA/AATS/PCNA/SCAI/STS focused update of the guideline for the diagnosis and management of patients with stable ischemic heart disease: A report of the American College of Cardiology/American Heart Association Task Force on practice guidelines, and the American Association for Thoracic Surgery, Preventive Cardiovascular Nurses Association, Society for Cardiovascular Angiography and Interventions, and Society of Thoracic Surgeons’, *Journal of the American College of Cardiology*, 64(18), pp. 1929–1949. Available at: <https://doi.org/10.1016/J.JACC.2014.07.017>.

Fischer, G.S. *et al.* (2008a) ‘MRI compatibility of robot actuation techniques - A comparative study’, in *International Conference on Medical Image Computing and Computer-Assisted Intervention*. Springer Verlag, pp. 509–517. Available at: https://doi.org/10.1007/978-3-540-85990-1_61/COVER.

Fischer, G.S. *et al.* (2008b) ‘MRI compatibility of robot actuation techniques--a comparative study’, in *Medical image computing and computer-assisted intervention : MICCAI ... International Conference on Medical Image Computing and Computer-Assisted Intervention*. Med Image Comput Comput Assist Interv, pp. 509–517. Available at: https://doi.org/10.1007/978-3-540-85990-1_61.

Fischer, G.S., Cole, G. and Su, H. (2011) ‘Approaches to creating and controlling motion in MRI’, in *Annual International Conference of the IEEE Engineering in Medicine and Biology Society*. . Annu Int Conf IEEE Eng Med Biol Soc, pp. 6687–6690. Available at: <https://doi.org/10.1109/IEMBS.2011.6091649>.

Ganesh, G. *et al.* (2004) ‘Dynamics and control of an MRI compatible master-slave system with hydrostatic transmission’, in *IEEE International Conference on Robotics and Automation*. Institute of Electrical and Electronics Engineers Inc., pp. 1288–1294. Available at: <https://doi.org/10.1109/ROBOT.2004.1308002>.

Goldman, M. (1982) ‘Ionizing Radiation and Its Risks’, *Western Journal of Medicine*, 137(6), p. 540. Available at: [/pmc/articles/PMC1274230/](https://pmc.ncbi.nlm.nih.gov/pmc/articles/PMC1274230/)?report=abstract (Accessed: 8 May 2023).

Green, J.D. et al. (2005) ‘Comparison of X-ray Fluoroscopy and Interventional MRI for the Assessment of Coronary Artery Stenoses in Swine’, *Magnetic resonance in medicine : official journal of the Society of Magnetic Resonance in Medicine / Society of Magnetic Resonance in Medicine*, 54(5), p. 1094. Available at: <https://doi.org/10.1002/MRM.20699>.

Groenhuis, V., Siepel, F.J. and Stramigioli, S. (2018) ‘Dual-Speed MR Safe Pneumatic Stepper Motors’, *Robotics: Science and Systems XIV* [Preprint]. Available at: <https://doi.org/10.15607/RSS.2018.XIV.030>.

Groenhuis, V. and Stramigioli, S. (2018) ‘Rapid Prototyping High-Performance MR Safe Pneumatic Stepper Motors’, *IEEE/ASME Transactions on Mechatronics*, 23(4), pp. 1843–1853. Available at: <https://doi.org/10.1109/TMECH.2018.2840682>.

Guo, Z. et al. (2018) ‘Compact Design of a Hydraulic Driving Robot for Intraoperative MRI-Guided Bilateral Stereotactic Neurosurgery’, *IEEE Robotics and Automation Letters*, 3(3), pp. 2515–2522. Available at: <https://doi.org/10.1109/LRA.2018.2814637>.

Guttmacher, A.E., Collins, F.S. and Nabel, E.G. (2003) ‘Cardiovascular Disease’, <https://doi.org/10.1056/NEJMra035098>. Edited by A.E. Guttmacher and F.S. Collins, 349(1), pp. 60–72. Available at: <https://doi.org/10.1056/NEJMRA035098>.

Holmes, D.R. et al. (2012) ‘2012 ACCF/AATS/SCAI/STS expert consensus document on transcatheter aortic valve replacement’, *Journal of the American College of Cardiology*, 59(13), pp. 1200–1254. Available at: <https://doi.org/10.1016/J.JACC.2012.01.001>.

Hwang, J., Kim, J. young and Choi, H. (2020) ‘A review of magnetic actuation systems and magnetically actuated guidewire- and catheter-based microrobots for vascular interventions’, *Intelligent Service Robotics*, 13(1). Available at: <https://doi.org/10.1007/S11370-020-00311-0>.

Khan, E.M. et al. (2013) ‘First experience with a novel robotic remote catheter system: AmigoTM mapping trial’, *Journal of interventional cardiac electrophysiology : an international journal of arrhythmias and pacing*, 37(2), pp. 121–129. Available at: <https://doi.org/10.1007/S10840-013-9791-9>.

Kim, K.P. and Miller, D.L. (2009) ‘Minimising radiation exposure to physicians performing fluoroscopically guided cardiac catheterisation procedures: a review’, *Radiation Protection Dosimetry*, 133(4), p. 227. Available at: <https://doi.org/10.1093/RPD/NCP052>.

King, A.P. and Eckersley, R.J. (2019) ‘Descriptive Statistics I: Univariate Statistics’, *Statistics for Biomedical Engineers and Scientists*, pp. 1–21. Available at: <https://doi.org/10.1016/B978-0-08-102939-8.00010-4>.

Krieger, A. et al. (2012) ‘Development and Evaluation of an Actuated MRI-Compatible Robotic System for MRI-Guided Prostate Intervention’, *IEEE/ASME transactions on mechatronics: a joint publication of the IEEE Industrial Electronics Society and the ASME Dynamic Systems and Control Division*, 18(1), pp. 273–284. Available at: <https://doi.org/10.1109/TMECH.2011.2163523>.

Krieger, A. et al. (2013) ‘Development and evaluation of an actuated MRI-compatible robotic system for MRI-guided prostate intervention’, *IEEE/ASME Transactions on Mechatronics*, 18(1), pp. 273–284. Available at: <https://doi.org/10.1109/TMECH.2011.2163523>.

Krueger, J.J. et al. (2006) ‘Magnetic resonance imaging-guided balloon angioplasty of coarctation of the aorta: a pilot study’, *Circulation*, 113(8), pp. 1093–1100. Available at: <https://doi.org/10.1161/CIRCULATIONAHA.105.578112>.

Lalande, V., Gosselin, F.P. and Martel, S. (2010) ‘Catheter steering using a Magnetic Resonance Imaging system’, *Annual International Conference of the IEEE Engineering in Medicine and Biology Society. IEEE Engineering in Medicine and Biology Society. Annual International Conference*, 2010, pp. 1874–1877. Available at: <https://doi.org/10.1109/IEMBS.2010.5627150>.

Lange, H.W. and Von Boetticher, H. (2006) ‘Randomized comparison of operator radiation exposure during coronary angiography and intervention by radial or femoral approach’, *Catheterization and cardiovascular interventions: official journal of the Society for Cardiac Angiography & Interventions*, 67(1), pp. 12–16. Available at: <https://doi.org/10.1002/CCD.20451>.

Lawrence, D.A. (1993) ‘Stability and Transparency in Bilateral Teleoperation’, *IEEE Transactions on Robotics and Automation*, 9(5), pp. 624–637. Available at: <https://doi.org/10.1109/70.258054>.

Lee, K.H. et al. (2018) ‘MR Safe Robotic Manipulator for MRI-Guided Intracardiac Catheterization’, *IEEE/ASME Transactions on Mechatronics*, 23(2), pp. 586–595. Available at: <https://doi.org/10.1109/TMECH.2018.2801787>.

Li, G. *et al.* (2021) ‘A Fully Actuated Robotic Assistant for MRI-Guided Precision Conformal Ablation of Brain Tumors’, *IEEE/ASME transactions on mechatronics : a joint publication of the IEEE Industrial Electronics Society and the ASME Dynamic Systems and Control Division*, 26(1), pp. 255–266. Available at: <https://doi.org/10.1109/TMECH.2020.3012903>.

Li, S. *et al.* (2012) ‘A catheterization-training simulator based on a fast multigrid solver’, *IEEE computer graphics and applications*, 32(6), pp. 56–70. Available at: <https://doi.org/10.1109/MCG.2012.32>.

Lindenroth, L. *et al.* (2016) ‘Stiffness-based modelling of a hydraulically-actuated soft robotics manipulator’, in *IEEE International Conference on Intelligent Robots and Systems*. Institute of Electrical and Electronics Engineers Inc., pp. 2458–2463. Available at: <https://doi.org/10.1109/IROS.2016.7759383>.

Manda, Y.R. and Baradhi, K.M. (2023) ‘Cardiac Catheterization Risks and Complications’, *StatPearls* [Preprint]. Available at: <https://www.ncbi.nlm.nih.gov/books/NBK531461/> (Accessed: 7 May 2023).

Maor, E. *et al.* (2017) ‘Current and Future Use of Robotic Devices to Perform Percutaneous Coronary Interventions: A Review’, *Journal of the American Heart Association: Cardiovascular and Cerebrovascular Disease*, 6(7). Available at: <https://doi.org/10.1161/JAHA.117.006239>.

Margielewicz, J., Gaśka, D. and Litak, G. (2019) ‘Modelling of the gear backlash’, *Nonlinear Dynamics*, 97(1), pp. 355–368. Available at: <https://doi.org/10.1007/S11071-019-04973-Z/FIGURES/9>.

Masamune, K. *et al.* (1995) ‘Development of an MRI-compatible needle insertion manipulator for stereotactic neurosurgery’, *Image Guided Surgery*, 1(4), pp. 242–248. Available at: <https://doi.org/10.3109/10929089509106330>.

Modan, B. *et al.* (2000) ‘Cancer following cardiac catheterization in childhood’, *International Journal of Epidemiology*, 29(3), pp. 424–428. Available at: <https://doi.org/10.1093/INTJEPID/29.3.424>.

Monfaredi, R., Cleary, K. and Sharma, K. (2018) ‘MRI Robots for Needle-Based Interventions: Systems and Technology’, *Annals of biomedical engineering*, 46(10), p. 1497. Available at: <https://doi.org/10.1007/S10439-018-2075-X>.

Moses, J.W. *et al.* (2003) ‘Sirolimus-eluting stents versus standard stents in patients with stenosis in a native coronary artery’, *The New England journal of medicine*, 349(14), pp. 1315–1323. Available at: <https://doi.org/10.1056/NEJMoa035071>.

Muller, L. *et al.* (2012) ‘Remote control catheter navigation: options for guidance under MRI’, *Journal of Cardiovascular Magnetic Resonance*, 14(1), p. 33. Available at: <https://doi.org/10.1186/1532-429X-14-33>.

Muthurangu, V. and Razavi, R.S. (2005) ‘The value of magnetic resonance guided cardiac catheterisation’, *Heart*, 91(8), p. 995. Available at: <https://doi.org/10.1136/HRT.2004.055137>.

Orme, N.M. *et al.* (2015) ‘Occupational Health Hazards of Working in the Interventional Laboratory: A Multisite Case Control Study of Physicians and Allied Staff’, *Journal of the American College of Cardiology*, 65(8), pp. 820–826. Available at: <https://doi.org/10.1016/J.JACC.2014.11.056>.

Panych, L.P. and Madore, B. (2018) ‘The physics of MRI safety’, *Journal of Magnetic Resonance Imaging*, 47(1), pp. 28–43. Available at: <https://doi.org/10.1002/JMRI.25761>.

Patel, N.A. *et al.* (2019) ‘System Integration and Preliminary Clinical Evaluation of a Robotic System for MRI-Guided Transperineal Prostate Biopsy’, *Journal of medical robotics research*, 4(2). Available at: <https://doi.org/10.1142/S2424905X19500016>.

Patel, N.A. *et al.* (2020) ‘An Integrated Robotic System for MRI-Guided Neuroablation: Preclinical Evaluation’, *IEEE transactions on bio-medical engineering*, 67(10), pp. 2990–2999. Available at: <https://doi.org/10.1109/TBME.2020.2974583>.

Prasad, K.N., Cole, W.C. and Hasse, G.M. (2004) ‘Health risks of low dose ionizing radiation in humans: a review’, *Experimental biology and medicine (Maywood, N.J.)*, 229(5), pp. 378–382. Available at: <https://doi.org/10.1177/153537020422900505>.

Price, D.L. *et al.* (2001) ‘Investigation of Acoustic Noise on 15 MRI Scanners from 0.2 T to 3 T’, *Journal of Magnetic Resonance Imaging*, 13(2), pp. 288–293. Available at: <https://doi.org/10.1002/1522-2586>.

Quirk, M.E. *et al.* (1989) ‘Anxiety in patients undergoing MR imaging’, *Radiology*, 170(2), pp. 463–466. Available at: <https://doi.org/10.1148/RADIOLOGY.170.2.2911670>.

Rafii-Tari, H. *et al.* (2016) ‘Reducing contact forces in the arch and supra-aortic vessels using the Magellan robot’, *Journal of vascular surgery*, 64(5), pp. 1422–1432. Available at: <https://doi.org/10.1016/J.JVS.2015.06.215>.

Riga, C. V. *et al.* (2013) ‘Robot-assisted fenestrated endovascular aneurysm repair (FEVAR) using the Magellan system’, *Journal of vascular and interventional radiology : JVIR*, 24(2), pp. 191–196. Available at: <https://doi.org/10.1016/J.JVIR.2012.10.006>.

Rolls, A.E. *et al.* (2014) ‘Robot-assisted uterine artery embolization: a first-in-woman safety evaluation of the Magellan System’, *Journal of vascular and interventional radiology : JVIR*, 25(12), pp. 1841–1848. Available at: <https://doi.org/10.1016/J.JVIR.2014.05.022>.

Rosebrock, A. (2018) *OpenCV Object Tracking - PyImageSearch*. Available at: <https://pyimagesearch.com/2018/07/30/opencv-object-tracking/> (Accessed: 15 May 2023).

Ross, A.M. *et al.* (1997) ‘Prevalence of spinal disc disease among interventional cardiologists’, *American Journal of Cardiology*, 79(1), pp. 68–70. Available at: [https://doi.org/10.1016/S0002-9149\(96\)00678-9](https://doi.org/10.1016/S0002-9149(96)00678-9).

Salvado, D. *et al.* (2014) ‘Collimator design for a clinical brain SPECT/MRI insert’, *EJNMMI Physics*, 1(S1). Available at: <https://doi.org/10.1186/2197-7364-1-S1-A21>.

Shaikh, Z.A., Eilenberg, M.F. and Cohen, T.J. (2017) ‘The Amigo™ Remote Catheter System: From Concept to Bedside’, *The Journal of Innovations in Cardiac Rhythm Management*, 8(8), p. 2795. Available at: <https://doi.org/10.19102/ICRM.2017.080806>.

Shokrollahi, E. *et al.* (2011) ‘In-vivo MRI and in-vivo electro-anatomical voltage map characteristics of infarct heterogeneity in a swine model’, *Annual International Conference of the IEEE Engineering in Medicine and Biology Society. IEEE Engineering in Medicine and Biology Society. Annual International Conference*, 2011, pp. 2792–2795. Available at: <https://doi.org/10.1109/IEMBS.2011.6090764>.

Shurab, M. *et al.* (2014) ‘Robotics in invasive cardiac electrophysiology’, *Expert review of medical devices*, 11(4), pp. 375–381. Available at: <https://doi.org/10.1586/17434440.2014.916207>.

de Silva, C.W. (2002) ‘Precision Motion Control: Design and Implementation Tan Kok Kiong, Lee Tong Heng,Dou Huifang, and Huang Sunan, Springer, London, U.K. 2001, 232 pp., ISBN: 1-85233-328-6’, *International Journal of Robust and Nonlinear Control*, 12(7), pp. 621–623. Available at: <https://doi.org/10.1002/RNC.662>.

Slicker, K. *et al.* (2016) ‘Daily cardiac catheterization procedural volume and complications at an academic medical center’, *Cardiovascular Diagnosis and Therapy*, 6(5), p. 446. Available at: <https://doi.org/10.21037/CDT.2016.05.02>.

Spanner, K. and Koc, B. (2016) ‘Piezoelectric Motors, an Overview’, *Actuators 2016, Vol. 5, Page 6*, 5(1), p. 6. Available at: <https://doi.org/10.3390/ACT5010006>.

Stoianovici, D., Patriciu, A., *et al.* (2007) ‘A new type of motor: Pneumatic step motor’, *IEEE/ASME Transactions on Mechatronics*, 12(1), pp. 98–106. Available at: <https://doi.org/10.1109/TMECH.2006.886258>.

Stoianovici, D., Song, D., *et al.* (2007) “MRI Stealth” robot for prostate interventions’, *Minimally invasive therapy & allied technologies : MITAT*, 16(4), pp. 241–248. Available at: <https://doi.org/10.1080/13645700701520735>.

Su, H. *et al.* (2012) ‘A MRI-guided concentric tube continuum robot with piezoelectric actuation: A feasibility study’, in *IEEE International Conference on Robotics and Automation*. Institute of Electrical and Electronics Engineers Inc., pp. 1939–1945. Available at: <https://doi.org/10.1109/ICRA.2012.6224550>.

Su, H. *et al.* (2016) ‘A Concentric Tube Continuum Robot with Piezoelectric Actuation for MRI-Guided Closed-Loop Targeting’, *Annals of biomedical engineering*, 44(10), pp. 2863–2873. Available at: <https://doi.org/10.1007/S10439-016-1585-7>.

Su, H. *et al.* (2022) ‘State of the Art and Future Opportunities in MRI-Guided Robot-Assisted Surgery and Interventions’, *Proceedings of the IEEE*, 110(7), pp. 968–992. Available at: <https://doi.org/10.1109/JPROC.2022.3169146>.

Tavallaei, M.A. *et al.* (2013) ‘A magnetic-resonance-imaging-compatible remote catheter navigation system’, *IEEE transactions on bio-medical engineering*, 60(4), pp. 899–905. Available at: <https://doi.org/10.1109/TBME.2012.2229709>.

Thukral, B.B. (2015) ‘Problems and preferences in pediatric imaging’, *The Indian Journal of Radiology & Imaging*, 25(4), p. 359. Available at: <https://doi.org/10.4103/0971-3026.169466>.

Tumanski, S. (2008) ‘Sensors and Actuators - Control System Instrumentation (de Silva, C.W.; 2007) [book review]’, *IEEE Instrumentation & Measurement Magazine*, 10(6), pp. 56–56. Available at: <https://doi.org/10.1109/MIM.2007.4428584>.

Venneri, L. *et al.* (2009) ‘Cancer risk from professional exposure in staff working in cardiac catheterization laboratory: insights from the National Research Council’s

Biological Effects of Ionizing Radiation VII Report', *American heart journal*, 157(1), pp. 118–124. Available at: <https://doi.org/10.1016/J.AHJ.2008.08.009>.

Wang, X. et al. (2018) 'Experimental validation of robot-assisted cardiovascular catheterization: model-based versus model-free control', *International journal of computer assisted radiology and surgery*, 13(6), pp. 797–804. Available at: <https://doi.org/10.1007/S11548-018-1757-Z>.

What Is Cardiac Catheterization (2022) *National Heart Lung and Blood Institute / NHLBI*. Available at: <https://www.nhlbi.nih.gov/health/cardiac-catheterization#> (Accessed: 17 May 2023).

Whitney, J.P. et al. (2014) 'A low-friction passive fluid transmission and fluid-tendon soft actuator', in *IEEE International Conference on Intelligent Robots and Systems*. Institute of Electrical and Electronics Engineers Inc., pp. 2801–2808. Available at: <https://doi.org/10.1109/IROS.2014.6942946>.

Whitney, J.P. et al. (2016) 'A hybrid hydrostatic transmission and human-safe haptic telepresence robot', in *IEEE International Conference on Robotics and Automation*. Institute of Electrical and Electronics Engineers Inc., pp. 690–695. Available at: <https://doi.org/10.1109/ICRA.2016.7487195>.

De Wilde, J.P. et al. (2007) 'Magnetic resonance imaging safety issues including an analysis of recorded incidents within the UK'. Available at: <https://doi.org/10.1016/j.pnmrs.2007.01.003>.

Zelias, A. et al. (2021) 'Percutaneous coronary intervention of a tortuous and complex circumflex lesion using the robotic CorPath GRX system', *Kardiologia Polska (Polish Heart Journal)*, 79(9), pp. 1044–1045. Available at: <https://doi.org/10.33963/KP.A2021.0057>.

Zhao, Y. et al. (2022) 'Remote vascular interventional surgery robotics: A literature review', *Quantitative Imaging in Medicine and Surgery*, 12(4), pp. 2552–2574. Available at: <https://doi.org/10.21037/QIMS-21-792/COIF>.

7. Appendices

7.1. Commercially Available Catheterisation Robots

Catheterisation robotic systems commercially available to date all utilise X-ray fluoroscopy for guiding catheter and guidewire manipulations during endovascular interventions. Notable among these systems are the *CorPath® GRX* platform, successor of the *CorPath® 200* (Corindus, Inc., Waltham, MA, USA; now acquired by Siemens Healthineers) as well as the *Sensei®* and *Magellan* platforms (Hansen Medical, Inc., Mountain View, CA, USA; now acquired by Auris Health). Additional systems include the *Amigo™ RCS* (Catheter Precision, Inc., Mount Olive, NJ, USA), the *Robocath R-One™* (Robocath, Rouen, France), and the *Niobe® ES Magnetic Navigation System* (Stereotaxis, Inc., St. Louis, MO, USA). A comprehensive overview of these systems is provided below:

The *CorPath® GRX* platform is tailored for percutaneous coronary interventions (PCI), including angioplasty and stenting, in addition to neurovascular (NVI) and peripheral vascular interventions (PVI). It employs a roller-based mechanism to concentrically clamp and manipulate—rotate and translate—the catheters and guidewires, offering a total of 5 degrees of freedom (DOF). The system's compatibility extends to various commercially available guidewires, third-party guiding catheters, and balloon/stent catheters; and its control interface comprises a joystick, buttons, and a touchscreen (Britz *et al.*, 2019; Zelias *et al.*, 2021; Berczeli *et al.*, 2022).

The *Sensei®* platform is primarily designed for EP procedures like cardiac mapping and ablation (Cruddas, Martin and Riga, 2021). The system is not compatible with off-the-shelf instruments and offers a 3 DOF remote control of a steerable guide catheter using a joystick (Shurrab *et al.*, 2014). Despite its reported stability and success in ablation procedures, certain mechanical issues have been noted. The *Magellan*, part

of Hansen Medical's next robot generation, is engineered for PVI and embolization procedures. The system demonstrated successful outcomes (Riga *et al.*, 2013; Rolls *et al.*, 2014; Rafii-Tari *et al.*, 2016) and was designed to operate with specialised robotic steerable catheters as well as standard guidewires. The *Magellan* also offers for a unique 7 DOF manipulation and is characterised by its implementation of a novel parallel two-conveyor-belt mechanism for the guidewire (Feng *et al.*, 2015). The design of this mechanism allowed for pure translation of the clamped guidewire when activated, with added rotation when the belts are sheared in opposite directions. Despite its promising records, its high operational costs and its incompatibility with third-party equipment have been significant drawbacks.

The *Amigo™ RCS* offers a more cost-effective option for EP procedures. It is compatible with a range of commercially available catheters and allow for 3 DOF manipulations controlled through a handheld device (Khan *et al.*, 2013; Shaikh, Eilenberg and Cohen, 2017).

The *Robocath R-One™* system, similar in design to the *CorPath® GRX* in terms of manipulation and loading of the catheter and guidewire as well as control interface, is engineered for PCI such as coronary angioplasty procedures. The system has demonstrated promising procedural success rates and is compatible with off-the-shelf balloon/stent catheters and guidewires (Chakravartti and Rao, 2019).

Lastly, the *Niobe® ES Magnetic Navigation System* utilises magnetic fields for navigation. It offers 3 DOF manipulation of customised magnetic catheters for ablation and cardiac mapping procedures, with the main advantage of allowing for steering torques to be directly generated at the catheter tip (Lalande, Gosselin and Martel, 2010). However, the large space requirement for its associated equipment and the prolonged setup time have been significant hurdles. The recently introduced Genesis system aims

to address these issues by providing a more compact and efficient setup (Hwang, Kim and Choi, 2020).

